Acta Astronautica 236 (2025) 810–827

Contents lists available at ScienceDirect

Acta Astronautica

journal homepage: www.elsevier.com/locate/actaastro

Actively pulsed dual heating in vaporizing liquid microthrusters: An integrated analysis combining numerical simulations and experiments

Angelica Maria Toscano [a], Daan Kortleven [b], Donato Fontanarosa [a,b], Miriam Basile [a], Guido Marseglia [a], Maria Rosaria Vetrano [b], Johan Steelant [b], Luca Francioso [c], Maria Grazia De Giorgi [a,*]

[a] Department of Engineering for Innovation, University of Salento, Lecce, Via per Monteroni 73100, Puglia (Southern Italy), Italy
[b] Department Of Mechanical Engineering, KU Leuven, Heverlee, Celestijnenlaan 300A postbus 2421, B-3001, Flemish Region, Belgium
[c] Institute for Microelectronics and Microsystems IMM-CNR, University of Salento, Lecce, Via per Monteroni, 73100, Puglia (Southern Italy), Italy

ARTICLE INFO

Keywords:
Micropropulsion
Vaporizing liquid microthruster
Flow boiling instabilities
Dual heating system
Small satellites

ABSTRACT

The advancement of Micro-Electro-Mechanical Systems technology has driven significant interest in micro-propulsion systems for small satellites (total mass < 10 kg) used in Earth observation missions, where precise attitude control is essential. Among the various microthruster concepts, vaporizing liquid microthrusters stand out for their simple design and ability to use liquid propellants, enabling compact and lightweight propulsion systems. These microthrusters can achieve nominal thrust levels between 0.1 and 10 mN with specific impulses exceeding 100 s when using water as a propellant. However, their Technology Readiness Level remains below 5 due to flow boiling instabilities, which significantly affect thermal and propulsive performance and limit device lifetime. To address these challenges, a novel dual-heating microthruster concept has been developed in collaboration with the Institute for Microelectronics and Microsystems of the National Research Council, based in Lecce (Italy) and KU Leuven (Belgium), led by the Aerospace Propulsion group at the University of Salento. The new design integrates two independent heating chambers, each equipped with dedicated heating elements and microsensing capabilities (thermistors and vapor quality capacitive sensors). This approach decouples the boiling and superheating phases, leading to improved control over the vaporization process and reducing thermal stresses. A numerical and experimental investigation was conducted to assess the impact of actively controlled dual pulsed heating on the devices thermal and propulsive behavior. A 1D numerical model was developed to analyze different heating strategies and optimize energy efficiency, while experimental validation provided critical insights into real-world performance. The results demonstrate that the dual-heating strategy enhances stability, increases operational efficiency, and extends the device's lifetime. These findings highlight the potential of adaptive control techniques in optimizing vapor–liquid microthruster operation, bringing microelectromechanical systems-based microthrusters closer to practical satellite applications.

1. Introduction

As the demand for more cost-effective and versatile space missions grows, there is increasing interest in small satellites due to their lower launch costs, quicker development times, and ability to perform a wide range of scientific and commercial tasks. The space industry is revolutionizing the approach to space missions, focusing on developing small satellites, such as nanosatellites and picosatellites, with a total mass of less than 20 kg and typical dimensions of $10 \times 10 \times 10 = 10\,\text{cm}^3$. The integration of secondary micropropulsion systems has become increasingly feasible thanks to recent advancements in micro-electro-mechanical systems (MEMS) technology. Among these innovations, vaporizing liquid microthrusters (VLMs) have emerged as a particularly promising solution. Interest in VLM propulsion has grown significantly due to the use of water as a propellant. As a green propellant, water is both safe and non-toxic, while still meeting essential performance requirements. These devices can generate thrust forces ranging from 0.1 mN to 10 mN, with a typical specific impulse between 50 and 100 s [1]. The evolution of silicon-based MEMS VLMs began in the late 1990s with the pioneering work of Mueller et al. [2–4]. This work achieved thrust between 50 μN and 200 μN with an average power consumption of 1–1.5 W. However, early designs faced challenges, particularly in achieving stable operating regimes and managing heat losses associated

* Corresponding author.
E-mail address: mariagrazia.degiorgi@unisalento.it (M.G. De Giorgi).

https://doi.org/10.1016/j.actaastro.2025.07.009
Received 28 February 2025; Received in revised form 3 July 2025; Accepted 4 July 2025
Available online 16 July 2025

Nomenclature

Symbols

$\%\delta CF_{\mathrm{TB}}$	Relative uncertainty of the corrected thrust measurement
$\%\delta I$	Relative uncertainty of the current measurement
$\%\delta P_{el}$	Relative uncertainty of the electrical power
α_l, α_v	Volume fractions of liquid and vapor
α_v	Vapour Volume fraction
$\chi_{\text{t-st}}$	Student's t multiplier for 95% confidence level
ΔH	Total enthalpy variation of the fluid
Δp	Pressure drop across the channel
Δs	Spatial discretization step
$\dot{m}$	Mass flow rate
$\dot{m}_{lv}$, $\dot{m}_{vl}$	Mass transfer rates due to evaporation and condensation
$\dot{Q}$, Q_1, Q_2	Heat transferred and power inputs in each zone
ϵ	Surface emissivity
$\epsilon_{\text{straingage}}$	Surface strain of the beam
$\eta_{heatloss}$	Heat loss efficiency
κ_{cond}	Thermal conductivity of the fluid
λ_v	Thermal conductivity of the vapor phase
μ_m	Mixture dynamic viscosity
σ	Stefan–Boltzmann constant
σ_{CF}	Corrected sample standard deviation
τ_{rise}	Rise time
τ_{set}	Settling time
$\vec{V}_v$	Velocity vector of the vapor phase
A_1, A_2	Heat exchange areas in zone 1 and zone 2
A_i/V	Interfacial area density between vapor and liquid phases
A_{cs}, A_{exchange}, A_{ext}, A_{e}	Cross-sectional, heat exchange, external, and exit areas
b	Width of the 3D-printed plate
C	Stiffness factor
c	Electrical capacitance in pF
CF_{TB}	Calibration factor of the thrust balance
d	Displacement
d_b	Diameter of vapor bubbles
D_h	Hydraulic diameter
E	Young's modulus
E_v	Specific internal energy of the vapor phase
E_{tot}	Energy consumption
f	Frequency
F, F_j, F_p	Thrust, jet force, pressure force
g_0	Gravitational acceleration
GF	Gauge factor
h	Thickness of the 3D-printed plate
h_{conv}	External convective heat transfer coefficient
h_{tot}	Total enthalpy
h_b	Heat transfer coefficient
H_{lv}	Latent enthalpy of evaporation
H_{nozzle}	Height of the VLM nozzle
H_{vl}	Latent enthalpy of condensation
I	Moment of inertia
I_H	Current crossing the heater
I_{sp}	Specific impulse
k_e, k_c	Evaporation and condensation coefficients
k_{cond}	Local thermal conductivity
k_{Si}	Thermal conductivity of silicon (device material)
l	Length of the 3D-printed plate
L_1, L_2, L_{ext}	Lengths of heating zones and external layer
$\dot{m}$	Mass flow rate
n	Number of time steps
Nu	Nusselt number
$\%OS$	Overshoot
p	Pressure
p_v	Pressure of the vapor phase
p_{amb}	Ambient pressure
P_{cs}	Perimeter of the heat exchange surface
P_{loss}	Power losses
P_{meas}	Measured power
P_{net}	Net power
P_{tot}	Total thermal power input
P_{avg}	Average power consumption
p_{DP15}	Measured absolute pressure
P_{el}	Supplied electrical power
p_e	Exit pressure
P_f	Fluid power
P_{start}	Fluid inlet pressure
$\dot{q}$	Heat flux
Q_{rad}, Q_{conv}, Q_{cond}	Radiative, convective, and conductive heat
R_s	Reliability ratio of the numerical simulation
R_H	Heater resistance
R_{RTD}	RTD resistance
S_1, S_{err}, S_{max}	Spatial, accumulated, and maximum discretization errors
$S_{\overline{\text{CF}}_{\text{TB}}}$	Corrected sample standard deviation of thrust measurements
T	Static Temperature
t	Time
T_l, T_v, T_{wall}, T_{fl}, T_{sat}, T_{ambient}	Liquid, vapor, wall, fluid, saturation and ambient temperatures
u	Axial velocity
$u_{\text{CF}_{\text{TB}}}$	Absolute uncertainty of the corrected thrust measurement CF_{TB}
u_e	Exit velocity of the fluid
V_{DP15}	Output voltage
V_{ex}	Excitation voltage of the Wheatstone bridge
V_{out}	Output voltage
W_{nozzle}	Width of the VLM nozzle
Z_{ch}	Channel height or depth

Subscripts

ext	Subscript denoting exit conditions (e.g., V_e, ρ_e, A_e)
0	Superscript denoting reference conditions (e.g., η_0)

1°	Superscript denoting the first heater temperature
2°	Superscript denoting the second heater temperature
avg	Subscript denoting average values (e.g., P_{avg})
heatloss	Subscript indicating heat loss efficiency (η_{heatloss})

Abbreviations

K_P, K_I, K_D	Proportional, integral and derivative PID gains
CFD	Computational Fluid Dynamics
CFL	Courant–Friedrichs–Lewy Number
CNR-IMM	Institute for Microelectronics and Microsystems of the Italian National Research Council
DAQ	Data Acquisition Module
DC	Direct Current
HTCC	high-temperature co-fired ceramic
LES	Large Eddy Simulation
LTCC	low-temperature co-fired ceramic
MEMS	Micro-Electro-Mechanical Systems
MOSFETs	Metal-Oxide-Semiconductor Field-Effect Transistors
PID	Proportional-Integral-Derivative Controller
RTDs	Resistive Temperature Detectors
SB	Scientific balance
TB	Thrust balance
VFS	Void Fraction Sensor
VLM	Vaporizing Liquid Microthruster

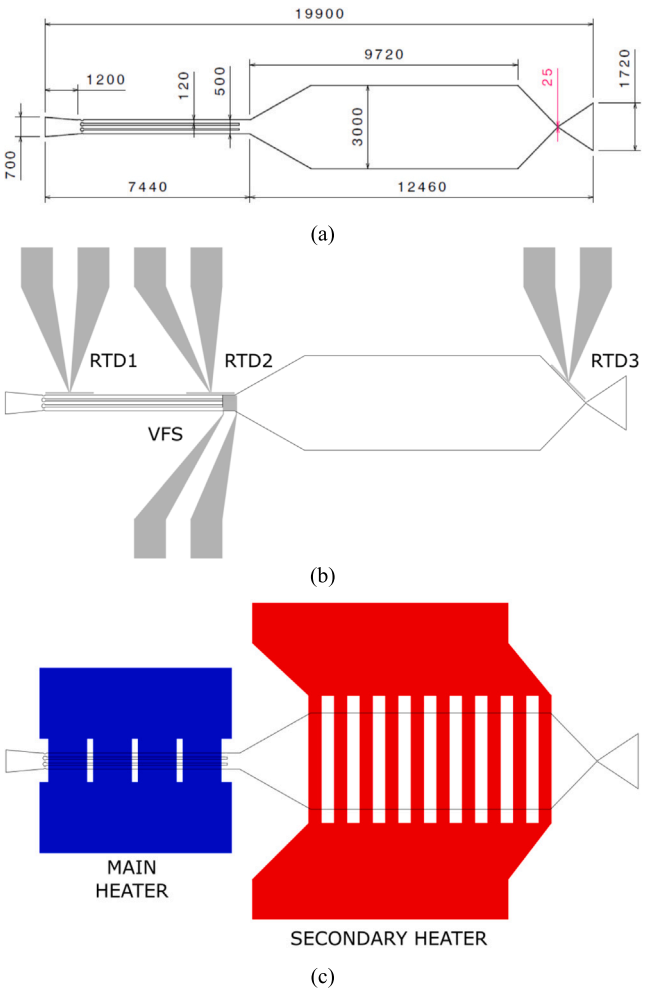

Fig. 1. VLM configuration: (a) sketch of the planar geometry of the Vaporizing Liquid Microthruster; (b) Position of temperature and void fraction sensors; (c) Configuration of the two heaters. (For interpretation of the references to colour in this figure legend, the reader is referred to the web version of this article.)

with packaging and the vaporization process, which prompted further design iterations. Over the years, various configurations have emerged, leveraging advancements in materials and fabrication techniques. Mukerjee et al. [5] developed a MEMS-based microthruster using wet anisotropic etching, where water served as the propellant and was preheated. While this configuration achieved thrust levels ranging from 0.15 mN to 0.46 mN, the average power remained high at 5 W. Other approaches, such as the design by Maurya et al. [6], aimed to lower the power consumption, achieving exceptionally low thrust of 5 μN to 120 μN using only 1 to 2.4 W of power. Building on these efforts, Kundu et al. [7] integrated two heaters within a single-channel VLM to improve heat distribution, which allowed for better thermal management and thrust performance, achieving 1 mN of T at 3.6 W of power. Pulsed heating strategies were explored by Ye et al. [8], achieving total impulses of 2 μNs with pulse power of 30 W in silicon-based microthrusters. Recent advancements by Silvia et al. [9] introduced integrated molybdenum heaters and temperature sensing mechanisms, providing further improvements in thrust performance, particularly for applications like CubeSats and PocketQubes. Non-silicon-based VLMs, such as low-temperature co-fired ceramic (LTCC) and high-temperature co-fired ceramic (HTCC) microthrusters, proposed by Karthikeyan et al. [10] and Cheah and Low [11], respectively, demonstrated improvements in specific impulse efficiency and power consumption. However, these designs often require more expensive production processes and lower resolution in pattern transfer compared to silicon-based MEMS technology. A significant issue in all microthruster designs remains the management of flow instabilities (particularly boiling in microchannels) that cause temperature and pressure oscillations, leading to fluctuating thrust, which compromises satellite control. Several researchers, including Chen et al. [12], have explored the complex two-phase flow patterns that occur, such as snake and vapor-droplet flows, and found that improper heating can lead to thruster failure or explosive boiling. Recent advancements, like the parallel channel systems proposed by Cen and Xu [13], represent significant progress in addressing these instabilities. Kwan et al. [14] further enhanced VLMs by operating them above the critical heat flux in the Leidenfrost boiling regime. Over the years, many strategies have been proposed to mitigate the negative effects of flow boiling instabilities. These include optimizing microchannel designs, improving thermal management with more effective heating and cooling systems, and using advanced control mechanisms.

2. Dual heating system: Design, experimental setup and performance analysis

2.1. Dual heating system: Design and Manufactoring

The Vaporizing Liquid Microthruster was designed and manufactured by the Institute for Microelectronics and Microsystems of the Italian National Research Council, in collaboration with the Aerospace Propulsion group of the University of Salento (Italy) and with support from KU Leuven (Belgium).

The microthruster was fabricated by adhesive bonding of different substrates (silicon and borosilicate glass) previously processed with thin film deposition and deep silicon etching; the oxidized 4-inch silicon wafer, which integrates the microfluidic network of the microthruster, includes the inlet port and outlet nozzle and heating chambers (160 μm channels depth). These features are transferred to silicon wafer by Inductively Coupled Plasma Etching process, that allows for detailed structuring and fine control of the channel dimensions and sidewalls slope. A 300 nm platinum thin film main heater was patterned on the backside of each chip before the dry etching step. A patterned high-temperature adhesive layer (100 μm thick) was finally deposited onto the borosilicate glass, which acts as a transparent sealing substrate with integrated heaters, RTD (Resistive Temperature Detectors) sensors and connections pads for heater driving and temperature monitoring. The planar geometry of the device is depicted in Fig. 1(a). The boiling chamber features three microchannels, each with a width of 120 μm and a length of 6000 μm. To mitigate boiling instabilities, each microchannel includes an inlet restriction. The purpose of incorporating inlet restrictions is to accelerate the flow and facilitate the removal of trapped vapor pockets. Downstream of the boiling chamber, a larger chamber measuring 3000 μm in width and 8000 μm in length is utilized to elevate the fluid to the required temperature for vaporization. The device ends with a converging-diverging nozzle, featuring a throat diameter of 25 μm. The embedded microelectronics, illustrated in Fig. 1(b), include two RTDs positioned at the inlet and outlet of the boiling chamber, with a third located at the inlet of the micronozzle. A large void fraction sensor (VFS) is installed at the micronozzle outlet to monitor the vapor content. The main objective is to achieve an optimal balance between the two heaters, minimizing overall wall overheating and ensuring the device operates within safer conditions, maintaining temperatures within the adhesive bonding limits (maximum 300 °C). The heating process is divided into two stages to accommodate significant changes in flow characteristics. Boiling occurs in the microchannels and is managed by the primary heater on the silicon layer, while superheating takes place in the rectangular chamber, controlled by the secondary heater on the glass side. The primary heater, depicted in blue with a thickness of 500 nm, is positioned at the base of the silicon layer, aligned with the boiling chamber. The secondary heater, shown in red with a thickness of 300 nm, is located on the glass layer, making direct contact with the fluid flow (Fig. 1(c)).

2.2. Experimental setup and methodology

Technological advances have significantly reduced the size of satellites, enabling micropropulsion technologies that operate within a thrust range of 0.1 mN to 10 mN. The need to accurately measure thrust in the micronewton to millinewton range presents unique challenges, as it requires a highly sensitive system capable of detecting extremely small forces. Environmental noise, often comparable in magnitude to the signal, can obscure measurements, while the precise and repeatable calibration of such small forces adds further complexity. A proper test bench was designed to measure the performance of a VLM. The water feed system designed for efficient propellant delivery to the device consists of a 50 ml PVC syringe, which dispenses the water through flexible PVC tubing. The system includes an NE-1000 syringe pump (accuracy: 0.5% of reading) that controls the flow rate, ensuring a constant mass flow of the propellant. Along the feeding line between the syringe and the VLM, the propellant flows through a 0.8 μm filter to remove potential particle contamination during liquid transfer and prevent micronozzle throat clogging and consequent flow blockage (see Fig. 2).

The main data acquisition system is based on a 4-slot chassis NI cDAQ-9174 by National Instrument. A K-type micro-thermocouple (accuracy: ±0.5 K) and a Validyne DP-15 variable reluctance differential pressure transducer coupled with a carrier demodulator type Validyne CD-15 measure the feeding temperature and pressure, respectively. As

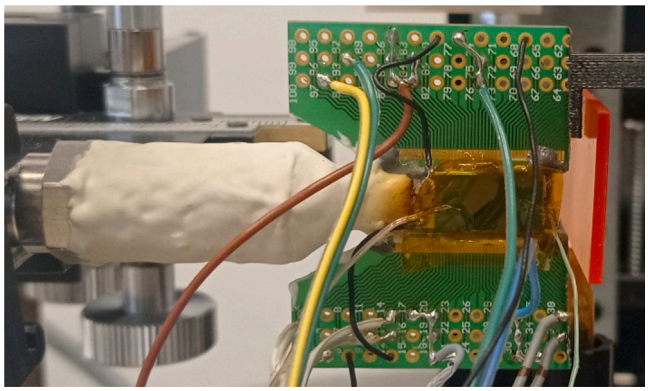

Fig. 2. Vaporizing Liquid Microthruster: final device arrangements.

described in [15], the pressure transducer is calibrated in a relative pressure range [0, 550] kPa using the MECP100 Pneumatic Hand Pump and the T-140-100PSI Hand-held Pressure Calibrator (resolution: 0.07 kPa; accuracy: 0.5% full scale). The resulting equation of the calibration curve is given in Eq. (1), with a coefficient of determination equal to $R^2 = 0.9998$ and a relative accuracy of ±0.5% of the reading:

$$p_{DP15}(V_{DP15}) = 55\,352 V_{DP15} + 101\,325 \tag{1}$$

where V_{DP15} is the output voltage (in V) of the pressure transducer and p_{DP15} is the measured absolute pressure (in Pa). The feeding temperature signal is recorded via the module NI-9211, while the feeding pressure signal is acquired using the module NI-9201 (resolution of 12 bits corresponding to a pressure resolution of 135 Pa); both signals are sampled at 10 Hz. The RTD sensors are connected to an NI 9217 data acquisition module, which measures their resistance at a sampling rate of 100 Hz. The NI 9217 uses a three-wire configuration with equal lead wire length to ensure accurate temperature readings. As described in [16], the calibration was performed by the CNR-IMM in a drying oven over the temperature range [297, 575] K, by installing a commercial PT1000 thin film element (accuracy: ±0.3 K) on the main microheater (i.e., on the bottom of the silicon substrate) and waiting for steady-state signals denoting the establishment of thermal equilibrium between the device and the oven environment. As a result, the linear correlation between the temperature T and the RTD resistance $R_{RTD}(T)$ was retrieved, with a coefficient of determination $R^2 = 0.9965$, as follows (2):

$$R_{RTD}(T) = R_{RTD,T_0}\left[1 + \alpha_{RTD,T_0}(T - T_0)\right] \tag{2}$$

where $\alpha_{RTD,T_0} = 0.0023\ K^{-1}$ and $R_{RTD,T_0} = 83.51\ \Omega$ at the reference temperature $T_0 = 293.15$ K. The resulting total uncertainty is ±1.8 K below 175 °C and less than ±1% of the reading above 175 °C. The void fraction sensor's signal is processed through a dedicated capacitance-to-digital converter, specifically the (EVAL-AD7152-EBZ, Analog Devices). This converter measures the sensor's capacitance and translates it into a digital signal. The resulting digital data is then analyzed by specialized software to determine the capacitance value. Concerning the pulsed dual heating systems, the two embedded micro-heaters are independently powered by a DC power supply model ISO-TECH IPS 2303, allowing for separate control of their power levels. Each heater is connected to the power supply via metal–oxide–semiconductor field-effect transistors (MOSFETs), model ICQUANZX. As described in [15], the MOSFETs regulate the power delivered to each heaters based on pulse width modulation switch (maximum frequency equal to 20 kHz), allowing for controlled power gating and precise control of the heating process. The pulsed dual heating control is implemented using the toolbox Labview and connecting MOSFETs module NI 9401. Concerning the supplied power measurements, the system incorporates two linear

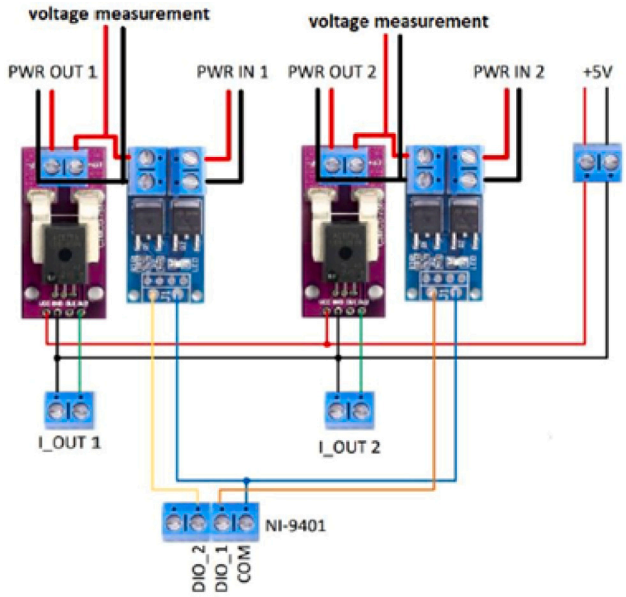

Fig. 3. Schematic of the pulsed dual heating electronics.

Hall effect current sensors HiLetgo ACS758LCB-050B-PFF-T (measuring range: 0 A – 50 A; response time: μs; bandwidth: 120 kHz; sensitivity: 40 mV/A; accuracy: ±1.2% of the reading). The sensors output is a voltage which is recorded via the oscilloscope R& S RTB2004(bandwidth: 300 MHz; 4 channels; sampling speed: 1.25 GS/s) using a voltage probe with attenuation factor 1:1. Additional voltage probes (same attenuation factor 1:1 as for the current measurements) located on the positive and negative leads of the VLM heaters were used to monitor the voltage applied to the two micro-heaters of the VLM. The schematic of the pulsed dual heating electronics is shown in Fig. 3.

The detailed description of the supplied electrical power P_{el} measurements in the presence of pulsed heating is provided in [15]. To estimate its relative uncertainty $\%\delta P_{\mathrm{el}}$, the expression relating the heater resistance R_H and the measured current crossing the heater I_H, i.e., $P_{\mathrm{el}} = R_H I_H^2$, is used. By neglecting the heater resistance as a design property intrinsically related to the high degree of repeatability of the manufacturing process, $\%\delta P_{\mathrm{el}}$ only depends on the relative accuracy of the current measurements, $\%\delta I$, which is equal to 1.2% of the reading as previously specified. As a result, $\%\delta P_{\mathrm{el}} = 2 \times \%\delta I = 2.4\%$ of the reading. It is worth underlining that each power measurement is averaged over a number of samples $N_{\mathrm{sample}} \geq 3$, to consider boiling-induced oscillations. A PID (Proportional-Integral-Derivative) feedback temperature control is applied to both main and secondary heaters, where $r(t)$ is the setpoint temperature, $y(t)$ is the measured temperature (RTD2 for the main due to its positioning and reduced susceptibility to boiling instabilities, and RTD3 for the secondary heater), and $u(t)$ is the controller output (i.e., the duty cycle). The feedback control is based on three main parameters: the proportional gain (K_p), integral time (K_i), and derivative time (K_d), which have been manually tuned to improve the control performance (smaller overshoot, faster settling time, higher stability). In the implemented PID control logic, this is done for each pulse and each heater. The whole PID control system is built via LabVIEW, allowing real-time monitoring and adjustment of the system's parameters, including PID tuning and reference temperatures, providing comprehensive control over the VLM's operation.

2.3. Thrust balance system

To accurately measure the thrust generated by the VLM, a dedicated thrust balance system was developed and positioned at the center of the experimental setup, as shown in Fig. 4.

The thrust balance system utilizes an impinging jet of the hot stream to exert force on a tilting plate, as illustrated in Fig. 5(a). The setup includes three micro-positioning stages each offering a resolution of 10 μm and an accuracy of ±5 μm. These stages are mounted on a 30 cm diameter circular optical plate and allow for precise adjustment of the VLM, micro-force sensor and safety stop arm. The safety stop arm protects the sensor during handling. The tilting mechanism features a 27 needle as a pivot point, supporting a 3D-printed plate. The 3D-printed plate is 2 mm thick (h), 50 mm long (l), and 20 mm wide (b) with a 0.9 mm diameter through-hole. The through-hole's axis is aligned with the plate's symmetry axis in the width direction. The entire tilting system is mounted vertically to facilitate gravity-assisted removal of condensed water during standard VLM operations, Fig. 5.

The micro-force sensor, illustrated in Fig. 5(b), features a cantilever beam made from silicon. This beam is equipped with two strain gauges: one on the top surface and one on the bottom. These strain gauges are configured in a Wheatstone half-bridge Type II arrangement. This setup allows the sensor to accurately measure force by detecting changes in strain on the cantilever beam when subjected to external forces. An applied force P at the free tip of the sensor plate (fixed at the opposite end) results in a tip displacement d. The relationship between P and d is given by Eq. (3), while Eq. (4) defines the stiffness factor C of the sensor plate. Here, E represents Young's modulus of the plate (1.6 × 105 N/mm), and I is the moment of inertia relative to the centroidal axis perpendicular to the applied force P.

$$d = \frac{Pl^3}{3EI} \tag{3}$$

$$C = \frac{P}{d} = \frac{Ebh^3}{4l} \tag{4}$$

The micro-force sensor signal is acquired by means of the data acquisition system cDAQ-9174 in combination with the strain gauges module NI-9237. By setting the nominal strain gauge resistance to 1000 Ω, and the gauge factor to 60 in accordance with its datasheet, the sensor measures the voltage across the half-bridge, which is then converted into strain by the NI-9237 module using (5).

$$\epsilon_{\mathrm{straingage}} = -\frac{2V_o ut}{V_{\mathrm{ex}}\,\mathrm{GF}} \quad \rightarrow \quad P = \frac{Ebh^2}{6l}\,\epsilon_{\mathrm{straingage}} \tag{5}$$

The determination of a calibration factor of the thrust balance, CF_{TB}, relating the true thrust to the measured thrust is needed to take into account thrust losses due to: (i) friction losses within the tilting system, and (ii) misalignment errors of the jet axis and the micro-force sensor with respect to the tilting system, mostly caused by manual operation and, hence, operator-dependent variability. To this purpose, a calibration investigation was performed by measuring the thrust produced by a pressurized air jet through a 27G needle with an inner diameter equal to 0.21 mm and a flat point style H. The feeding pressure of the air jet was varied using a pneumatic valve in the relative pressure range 0 kPa–550 kPa, and measured with the same relative pressure transducer Validyne DP15, previously calibrated. The true jet thrust was measured using the scientific balance (SB), model Acculab Atilon (measuring range: 0 mgf–220 mgf; accuracy: 0.1 mgf), with the needle jet positioned vertically downward, perpendicular and centered with respect to the measuring plate, and the tip located 2 mm away from the measurement plate, Fig. 6.

The same jet thrust tests were repeated using the designed thrust balance (TB). Therefore, the relationship between the applied feeding pressure and the measured thrust was retrieved by linear regression for both measurements, as shown in Fig. 7.

As a result, CF_{TB} was then estimated as the ratio between the slopes of the linear regression equations of the analytic balance and the designed thrust balance, i.e.,

$$CF_{\mathrm{TB}} = \frac{\text{SB curve slope}}{\text{TB curve slope}}.$$

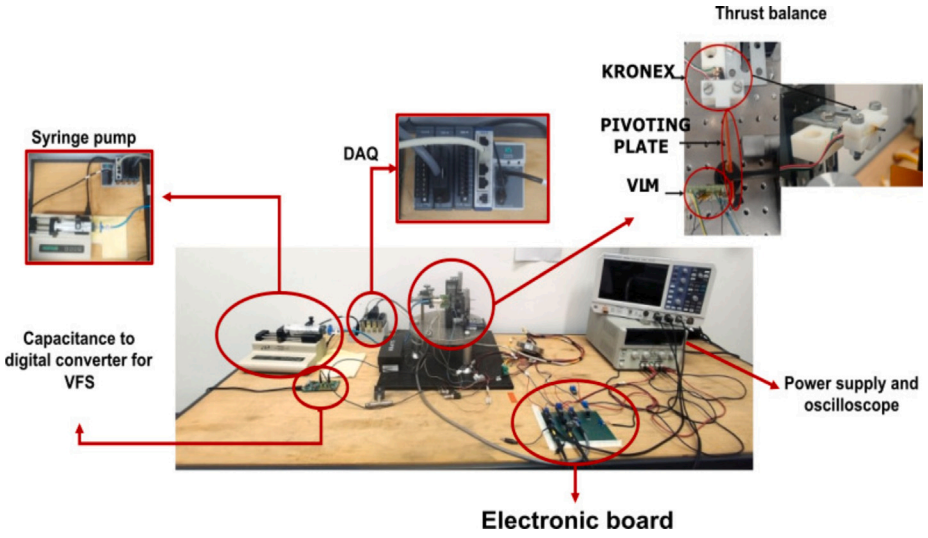

Fig. 4. The full experimental setup.

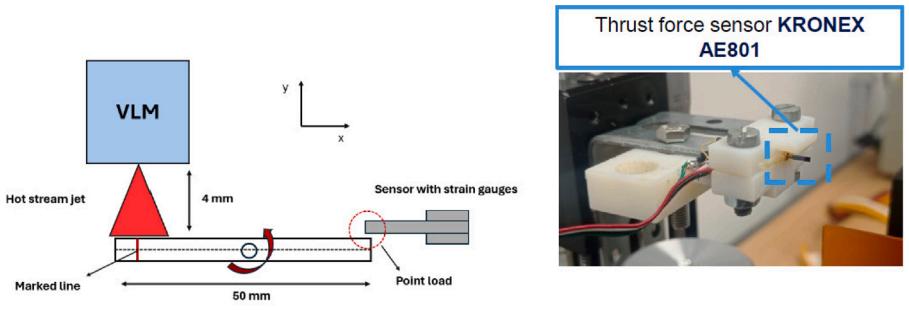

(a) (b)

Fig. 5. Micro-force sensor Kronex AE801: sketch and final configuration.

(a) (b)

Fig. 6. Measurement of the true thrust: experimental apparatus and jet-balance configuration.

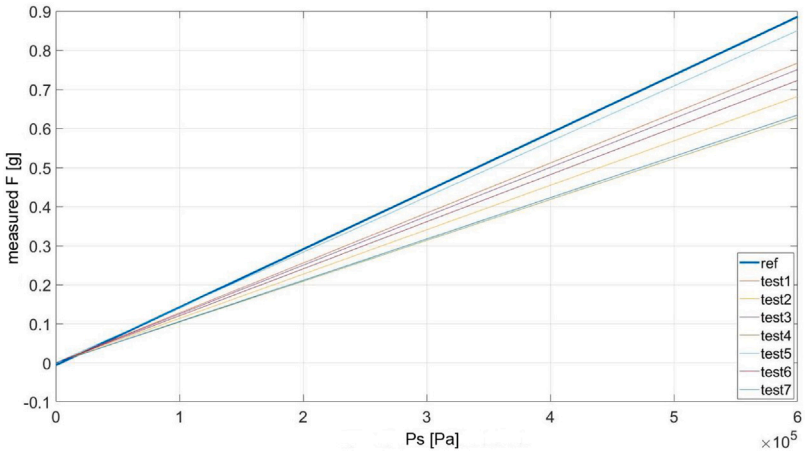

Fig. 7. A graph comparing the force measured by the thrust balance and the reference force of the scientific balance as a function of needle pressure. The graph displays first-degree polynomial fits derived from the data.

To strongly estimate the accuracy, the operator realigned the thrust balance and repeated the calibration process $N_{\mathrm{CF}} = 8$ times, resulting in an average calibration factor $\overline{CF}_{\mathrm{TB}}$ equal to 1.835. As suggested in [17], the precision index of such a mean value was computed as

$$S_{\overline{CF}_{\mathrm{TB}}} = \frac{\sigma_{\mathrm{CF}}}{\sqrt{N_{\mathrm{CF}}}} = 0.082,$$

where σ_{CF} is the corrected sample standard deviation. This value was then used to estimate the uncertainty of CF_{TB} as

$$u_{CF_{\mathrm{TB}}} = \chi_{t\text{-st}} \cdot S_{\overline{CF}_{\mathrm{TB}}},$$

where $\chi_{t\text{-st}} = 2.365$ is the Student's t-multiplier for 95% confidence and degrees of freedom $(N_{\mathrm{CF}} - 1)$. The final uncertainty in CF_{TB} is 0.193, corresponding to a relative uncertainty in the measured thrust equal to 10.5% of the reading.

2.4. Testing results

This section presents an analysis of experimental results obtained under ambient conditions, using water as the propellant, with particular attention given to the initial startup performance of the VLM. Initially, a flow rate of 13 ml/h was set on the syringe pump to ensure smooth delivery of water to the device. This flow rate, while set on the pump, does not directly represent the actual mass flow rate within the device. Once the RTD 2 sensor indicated that the temperature had dropped to the boiling point, and the void fraction sensor confirmed the presence of water inside the device, the values of the electrical capacitance c in [pF] relative to time increased on the graph (Fig. 8), indicating a change in the system's conditions. Therefore the mass flow rate on the syringe pump was adjusted to a lower value. Subsequently, the pressure — defined as the differential pressure relative to ambient conditions — gradually increased and stabilized around 192–193 kPa after approximately 10 min. The behavior of pressure and temperature measurements at the startup has been shown in Fig. 9.

In the experiments conducted during this campaign, three devices, with the same manufacturing process and geometry, were tested under identical conditions. Specifically, the heaters for all devices were set to identical temperatures, to ensure consistent operating conditions across all tests. These temperature settings ($T_{1°heater}$ and $T_{2°heater}$) are detailed in Table 1. This standardized approach facilitated a direct comparison of the devices' performance by maintaining uniform heating conditions throughout the experiment. By analyzing the measured power P_{meas} and accounting for known power losses P_{loss}, the mass flow rate $\dot{m}$ was estimated using Eq. (6).

$$P_{\mathrm{net}} = P_{\mathrm{meas}} - P_{\mathrm{loss}} \quad \rightarrow \quad \dot{m} = \frac{P_{\mathrm{net}}}{h_{\mathrm{tot}}} \tag{6}$$

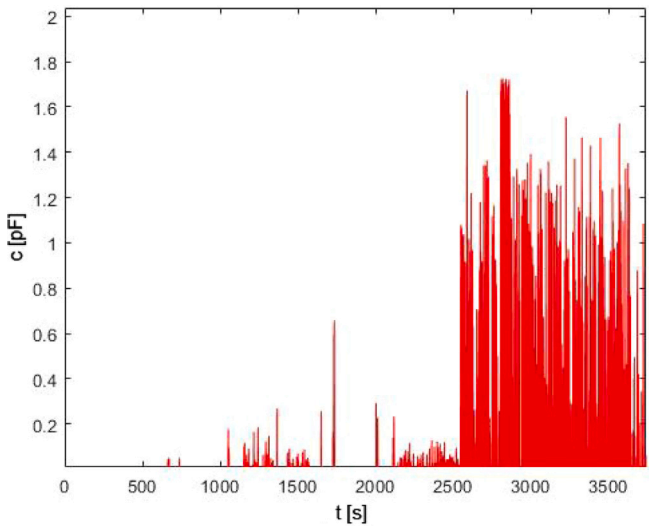

Fig. 8. Data from void fraction sensor, higher capacity means a higher liquid amount in the fluid.

Table 1
Summary of test conditions for the three identical devices.

Test	Device	$T_{1°heater}$ [°C]	$T_{2°heater}$ [°C]
Test 1	Device 1	120	150
Test 2	Device 1	120	150
Test 3	Device 2	120	150
Test 4	Device 3	120	150
Test 5	Device 3	120	150

where h_{tot} is the total enthalpy required for the heating process.

Variations in mass flow rates observed between Test 1 and Test 2 on the same device can be largely attributed to the device's stabilization period. Although the device was initially set to a constant mass flow rate of 3 ml/h and given time to stabilize, it is possible that the device required additional time to fully reach optimal operating conditions. This stabilization period could have led to discrepancies in the measured mass flow rate between different tests. Despite the initial variations, the tests conducted with a higher flow rate of 13 ml/h, which was later reduced to the operating condition, resulted in pressure levels that were consistent with those observed when starting directly at 3 ml/h. This indicates that, once stabilized, the device performed consistently, and the variations between tests were primarily due to

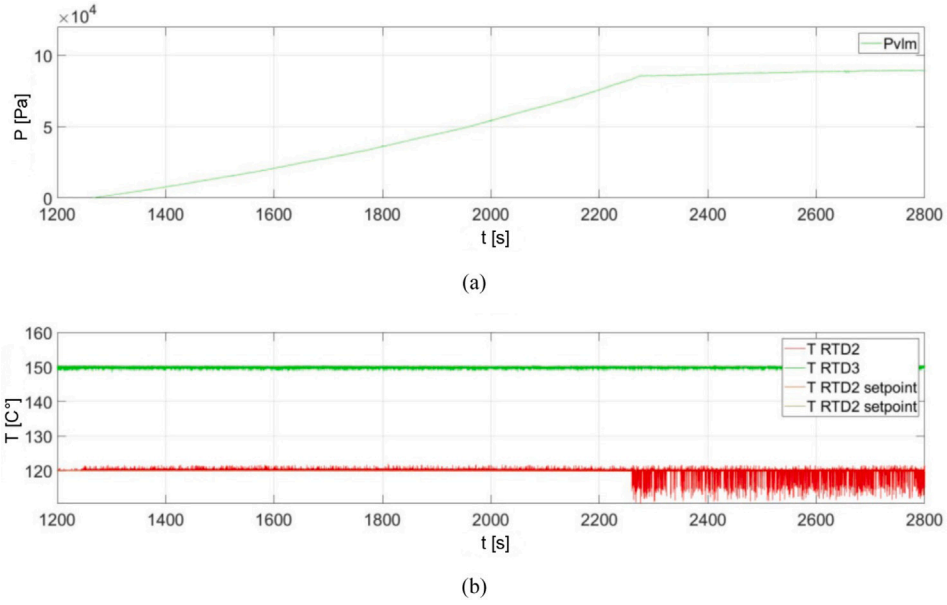

Fig. 9. Start up behavior of experimental results: Pressure (Pvlm is the differential pressure inside the device compared to the ambient pressure) and temperature data inside the vaporizing liquid microthruster.

Table 2
Performance parameters measured during tests.

Test	$\dot{m}$ [kg/s]	F [mN]	Isp [s]	P_{net} [W]	τ [m/W]	$\eta_{heatloss}$	η_0
Test 1	1.60e−6	1.8	112.00	4.276	0.41	0.525	0.45
Test 2	1.91e−6	2.4	127.79	5.086	0.47	0.577	0.59
Test 3	1.49e−6	1.1	77.71	3.962	0.29	0.578	0.21
Test 4	1.94e−6	2.5	132.44	5.165	0.49	0.641	0.63
Test 5	1.90e−6	2.4	128.34	5.064	0.47	0.636	0.60

the time needed for the device to adjust to the set mass flow rate rather than significant performance differences. Consequently, due to the variations in the mass flow rate, a lower specific impulse value of 112 s was observed in test 1. The parameter $\eta_{heatloss}$ (Table 2), determined using Eq. (7), quantifies the amount of power dissipated as heat into the surrounding environment.

$$\eta_{\text{heatloss}} = \frac{P_{\text{net}}}{P_{\text{net}} + P_{\text{loss}}} \tag{7}$$

For Test 3 with Device 2, a lower pressure drop was observed, Fig. 10(b). The net power (see Table 2) is very low, leading to a lower mass flow rate, reducing thrust, and a decreased the specific impluse with a value of 77.71 s. The reduction in performance may be attributed to the device's lower efficiency at lower mass flow rates. When the mass flow rate is low, the device struggles to transfer power effectively to the liquid. This can occur for two main reasons: the nozzle may be clogged, resulting in a reduced flow within the device, or there may be flow losses within the system that further diminish the mass flow rate. Additionally, if the flow is not fully vaporized at the nozzle due to low power consumption, it can lead to insufficient thrust. These combined factors can significantly impact the overall efficiency and effectiveness of the system. Fig. 10(a) illustrates the pressure and thrust variations during Test 3 with Device 2. The thrust measurements display a distinct initial spike shortly after the temperature is increased to operational conditions. This spike, evident in all measurements, is attributed to residual liquid from previous tests. As this residual liquid evaporates, it causes a temporary increase in thrust. Once the residual liquid has completely evaporated, several minutes are required for the new liquid to reach the device and stabilize its performance. At approximately 690 s, a sudden drop in pressure is observed, stabilizing around 20 kPa, accompanied by a marked increase in thrust. This change indicates a shift to stable operation with the new liquid. Prior to the pressure drop, an excessive water flow rate impeded the proper evaporation of the fluid, resulting in lower-than-expected thrust. After the pressure drop, the reduction in flow rate enabled complete vaporization of the fluid, which led to a notable increase in thrust. Fig. 10(b) displays the thrust and pressure trends for Test 4 with Device 3. Initially, a thrust spike is observed, followed by a gradual increase as the pressure stabilizes.

3. Numerical analysis: Validation and insight into device flow dynamics

3.1. Analysis of the impact of heating configuration on microthruster performance

The Computational Fluid Dynamics analysis was primarily conducted to validate the experimental results and ensure an accurate representation of the device's behavior. Additionally, the analysis provided valuable insights into the internal flows and dynamics of the microthruster, such as velocity fields, pressure distributions, temperature gradients, and phase change behaviors, which are difficult to measure experimentally. Furthermore, through numerical analysis, the performance of the devices related to the heater configuration was verified, demonstrating the optimal device arrangement. The use of numerical analysis offers an efficient and reliable approach for obtaining preliminary results, particularly when the work technology is highly sensitive, and the manufacturing process is neither fast nor dependable. This is crucial in cases where the high probability of breakage limits the availability and practicality of the device.

3.1.1. Computational settings

The prototype was digitally replicated using CAD software to generate a detailed 3D model. CFD simulations were carried out in ANSYS Fluent using a pressure-based solver with an implicit scheme to resolve the system's flow and thermal behavior. To reduce computational cost while preserving key physical phenomena, several simplifying assumptions were made: the fluid was considered incompressible and Newtonian, and saturation temperature was treated as constant due to negligible axial pressure variation. Both steady-state and transient simulations were conducted to evaluate the effects of continuous and pulsed heating. Two-phase flow and phase-change phenomena within the microchannels were modeled using the Eulerian–Mixture

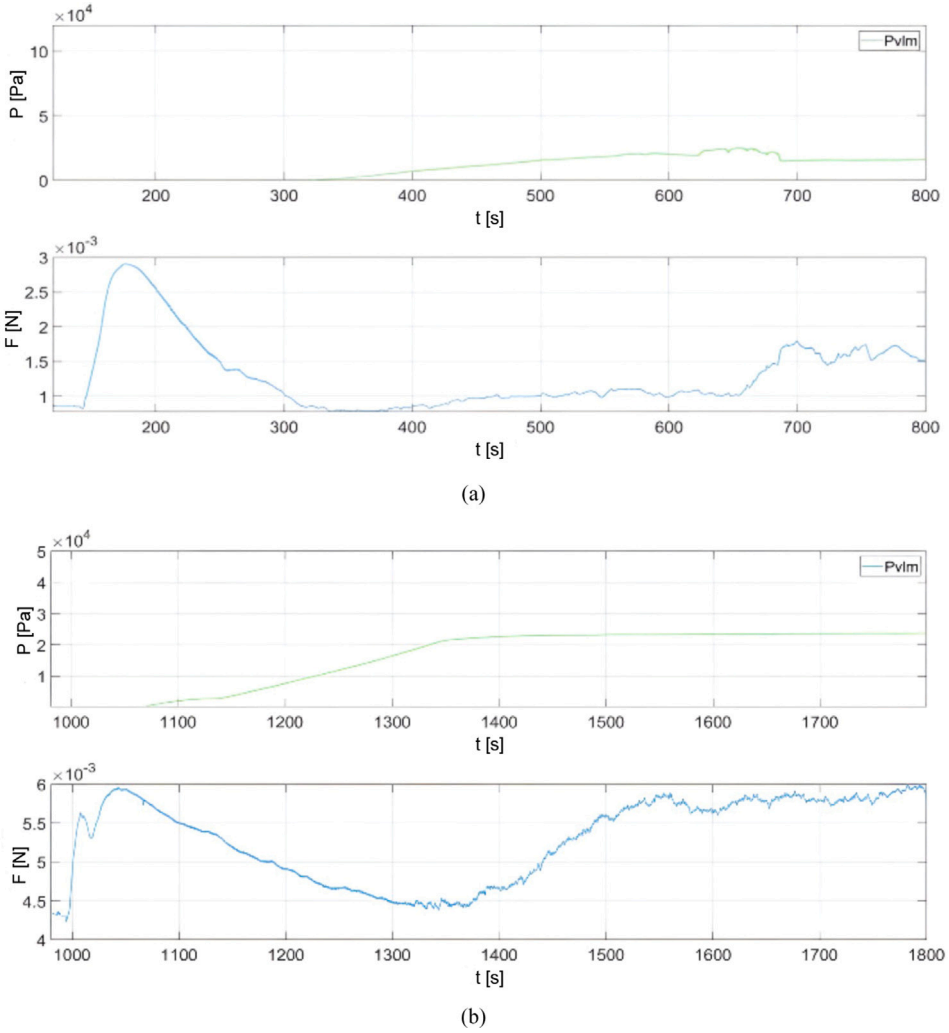

Fig. 10. Pressure and thrust trends for two different tests: (a) Pressure and thrust trends for Test 3 conducted with device 2; (b) Pressure and thrust trends for Test 4 conducted with device 3.

approach, which treats liquid and vapor phases as interpenetrating continua, ensuring stable and efficient handling of interphase interactions without interface tracking. The Lee phase change model [18] was adopted to simulate evaporation and condensation, with mass transfer driven by local deviations from saturation temperature and pressure. The full formulation, including thermodynamic details, is provided in Section 3.2.

Turbulence was modeled using the realizable k-ϵ approach, selected for its balance between accuracy and computational efficiency in predicting flow separation and heat transfer in confined microchannels. Although the k-ω SST model offers improved near-wall accuracy and is well-suited for boundary-layer-resolved simulations, the realizable k-ϵ model was adopted due to its favorable compromise between accuracy and computational cost in weakly turbulent microchannel flows. Compared to LES, which resolves fine-scale turbulence at high computational cost, the k-ϵ model offers a more efficient alternative for mesh and parametric studies, with acceptable accuracy in global thermal predictions.

To closely replicate the experimental conditions, an iterative procedure was employed to determine the optimal inlet pressure, ensuring that the simulated mass flow rate accurately matched the measured values. Two target flow rates were considered: 1.90×10^{-6} kg/s and 1.70×10^{-6} kg/s, corresponding to Tests 1 and 4 in Table 2, respectively. These values were selected based on representative operating points from the experimental campaign. Several simulation runs were performed, systematically adjusting the inlet pressure until the desired mass flow rate was reached. This method allowed for close matching between the simulated and experimental mass flow rates, ensuring consistency in the results. The final inlet pressure required to achieve the target mass flow rate was identified and applied. The input temperature was set at 300 K. A boundary condition for the outlet pressure was applied at the exit of the nozzle, maintaining an ambient pressure of 101 325 Pa (ambient atmospheric pressure (p_{amb})) with a backflow temperature set at 300 K. The walls of the microchannels and nozzle were assigned non-slip boundary conditions, with heat flux applied based on the experimental power input from the heaters. Specifically, the primary heater temperature was set to 120 °C, while the secondary heater operated at 150 °C, replicating the conditions detailed in Table 1. In the single-heater configuration, the primary heater temperature was increased to 150 °C, while the secondary heater was deactivated (maintained at 20 °C).

The computational geometry, including the inlet, microchannels, and nozzle, was carefully reconstructed to maintain consistency with the physical prototype. A structured hexahedral mesh was generated, applying localized refinement in critical regions such as microchannels and the converging-diverging nozzle, where sharp gradients in temperature, pressure, and velocity are expected. A mesh sensitivity analysis was performed to ensure grid independence, evaluating three different mesh densities: a coarse mesh (~1.3 million cells), medium mesh (~1.6 million cells) and fine mesh (~2.5 million cells). Key performance

parameters, including mass flow rate, temperature distribution, and pressure drop, were compared in these resolutions. The results stabilized between the medium and fine mesh, showing a variation of less than 1%, confirming that the medium-density mesh (~1.6 million cells) provided the best balance between accuracy and computational cost. The numerical discretization schemes were selected to ensure the stability and accuracy of the solution. The momentum, energy and turbulence equations were discretized using a second-order upwind scheme, while the pressure-velocity coupling was handled via the SIMPLE algorithm in steady-state simulations and the PISO algorithm for transient cases. A first-order implicit backward Euler scheme was used for time integration in transient simulations, employing adaptive time-stepping with a starting time step of 1e−6 s, ensuring that the Courant–Friedrichs–Lewy (CFL) number remained below 1 in critical regions. The convergence criteria were rigorously defined, requiring residuals to fall below 10^{-3} for mass, momentum, and turbulence equations, and below 10^{-6} for the energy equation. In addition to residual monitoring, critical physical quantities, including thrust, mass flow rate, and local temperature distributions, were continuously tracked to verify solution stability and physical consistency. The simulations were validated by comparing the predicted thrust, mass flow rate, and temperature profiles with experimental measurements taken at key locations within the device. The thrust predicted by the simulation was within 5% of the experimental values, confirming the reliability of the numerical model. A sensitivity analysis on the phase change parameters (e.g., latent heat of vaporization, interfacial mass transfer) further ensured the accuracy of the two-phase flow dynamics.

3.2. Two-phase evaporation modeling

The two-phase flow and phase change phenomena are modeled using the *mixture multiphase framework* combined with the *Lee model* [18] for evaporation and condensation. This approach treats both liquid and vapor as interpenetrating continua and is particularly suited for dense and thermally coupled flows in microchannels, where the computational cost of Lagrangian tracking of individual droplets is prohibitive.

The mass conservation equation governing the vapor phase in the Lee model is given by:

$$\frac{\partial}{\partial t}(\alpha_v \rho_v) + \nabla \cdot (\alpha_v \rho_v \vec{V}_v) = \dot{m}_{lv} - \dot{m}_{vl} \tag{8}$$

where α_v is the vapor volume fraction, ρ_v is the vapor density, and $\vec{V}_v$ is the vapor phase velocity. The terms $\dot{m}_{lv}$ and $\dot{m}_{vl}$ represent the mass transfer rates for evaporation and condensation, respectively. These are calculated based on the local temperature deviation from the saturation temperature T_{sat}, using the empirical relations:

The phase change mass transfer rates are defined according to local deviations from the saturation temperature. Specifically, the evaporation rate (for $T_l > T_{\text{sat}}$) and the condensation rate (for $T_v < T_{\text{sat}}$) are given by the following expressions:

$$\dot{m}_{lv} = k_e \cdot \alpha_l \rho_l \cdot \frac{T_l - T_{\text{sat}}}{T_{\text{sat}}} \qquad \text{(Evaporation)} \tag{9}$$

$$\dot{m}_{vl} = k_c \cdot \alpha_v \rho_v \cdot \frac{T_{\text{sat}} - T_v}{T_v} \qquad \text{(Condensation)} \tag{10}$$

Here, k_e and k_c are empirical coefficients (inverse of the relaxation time) that govern the rates of evaporation and condensation, respectively. These parameters must be calibrated to match experimental observations. Although a default value of 0.1 s^{-1} is commonly adopted, the coefficient can vary up to 10^3 s^{-1}, depending on fluid properties, bubble size, and the prevailing thermodynamic conditions [19]. In the present study, we adopted the values $k_e = k_c = 0.1$ s^{-1}, in line with prior work on microscale evaporation modeling [20]. This choice is justified by the relatively small scale of the microchannels, the absence of strong superheating or subcooling conditions, and the limited bubble growth dynamics due to the confined geometry. Under these conditions, phase change is assumed to occur in a quasi-equilibrium regime, where the temperature deviations from saturation are moderate and the system responds promptly to thermal input. Using a higher value would imply more aggressive phase transition kinetics, which could lead to numerical instability or overprediction of vapor generation. The adopted value thus provides a stable and physically reasonable compromise, aligned with typical recommendations for confined microchannel flows operating under moderate thermal loads. The variables α and ρ denote the local volume fraction and density of each phase, respectively.

The corresponding energy conservation equation for the vapor phase is expressed as:

$$\frac{\partial}{\partial t}(\alpha_v \rho_v E_v) + \nabla \cdot (\alpha_v \rho_v E_v \vec{V}_v) = \nabla \cdot (\alpha_v \lambda_v \nabla T_v) + \nabla \cdot (\alpha_v p_v \vec{V}_v) + \dot{m}_{lv} H_{lv} - \dot{m}_{vl} H_{vl} \tag{11}$$

Here, E_v is the specific internal energy of the vapor phase, λ_v is its thermal conductivity, p_v is the vapor pressure, and H_{lv}, H_{vl} represent the latent enthalpies associated with evaporation and condensation, respectively. The source terms $\dot{m}_{lv} H_{lv}$ and $\dot{m}_{vl} H_{vl}$ account for energy exchange due to phase change. This formulation ensures consistency with the mass transfer model and captures the thermal effects of phase transition within the mixture framework.

In the mixture model, the interfacial area density A_i/V is approximated assuming a dispersed regime of vapor bubbles with uniform diameter d_b, using the relation:

$$\frac{A_i}{V} = \frac{6 \alpha_v \alpha_l}{d_b} \tag{12}$$

In the present simulations, a constant bubble diameter of $d_b = 1 \times 10^{-5}$ m was assumed, consistent with typical estimates for confined microscale boiling flows.

Although the present model effectively captures the overall mass and energy exchange between phases, it relies on the assumption of local thermodynamic equilibrium and does not account for non-equilibrium interfacial phenomena. In particular, it neglects the influence of local vapor partial pressure and interface kinetics on mass flux, limiting its ability to represent fine-scale droplet dynamics where curvature and temperature gradients play a significant role [21–24].

In the Eulerian formulation adopted here, droplets are not individually tracked. Instead, phase interactions are governed by volume fraction and interfacial area density fields. While one could estimate the number of physical droplets by assuming a droplet size distribution and total injected mass, such analysis lies beyond the scope of this work.

The two-phase flow is thus treated as a continuum mixture, rather than a polydisperse or Lagrangian spray. This approach captures the macroscopic features of evaporation and condensation, but not the detailed behavior of individual droplets. More advanced models—such as those described in [23,24]—resolve droplet size distributions and track particle dynamics using a Lagrangian framework, offering a more detailed representation of spray behavior.

Future developments may include the integration of non-equilibrium interfacial models, population balance methods, or Lagrangian tracking schemes to improve phase-change resolution, especially under conditions involving strong thermal gradients, fast transients, or microgravity environments.

3.2.1. Numerical results and analysis of heating configurations

This section analyzed the thermal and phase-change behavior of the device under different heating configurations. By examining temperature and vapor fraction contours, the impact of using one or two heaters on device performance is highlighted. The study focuses on how the heating arrangement influences the efficiency of vaporization and, consequently, the overall thrust performance. The results provide valuable insights into the advantages of a dual-heater setup compared to a single-heater configuration. Fig. 11(a) illustrates the temperature distribution along the device walls for the dual-heater configuration,

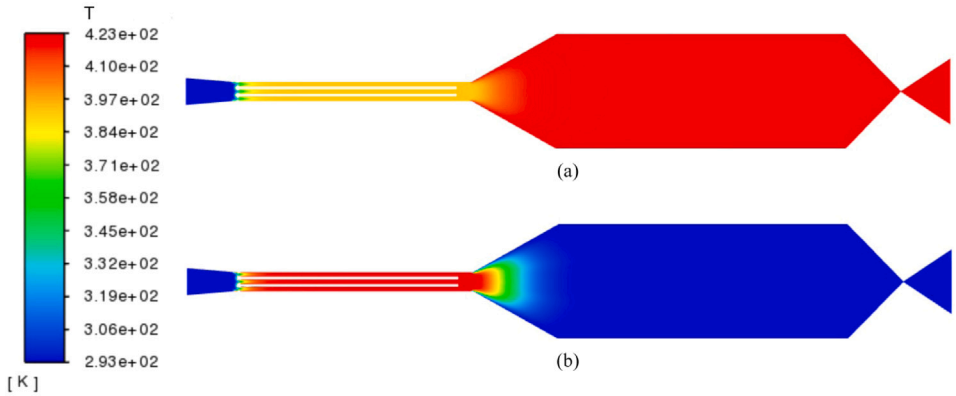

Fig. 11. Numerical temperature distribution throughout the device: (a) dual heating strategy; (b) single heating strategy.

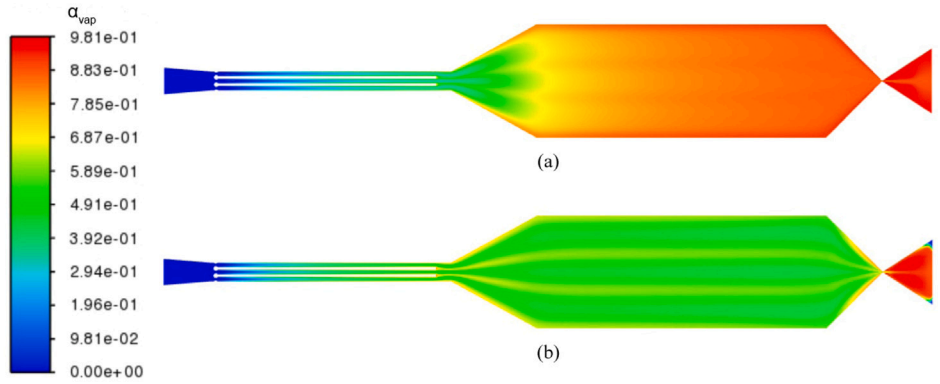

Fig. 12. Numerical vapor fraction distribution throughout the device: (a) dual heating strategy; (b) single heating strategy.

revealing a well-defined thermal gradient near the first heating element, where the incoming flow is rapidly heated before propagating downstream. The second heater further enhances thermal uniformity, ensuring that the working fluid reaches a higher temperature before exiting the nozzle, where it attains a final temperature of 423 K. In Fig. 11(b), is shown the temperature contour of the device considering only a single heater. Compared to the dual-heater case, thermal penetration is significantly lower, with the temperature reaching only 306 K before the nozzle. The heat input is concentrated in a smaller region, leading to a less effective temperature distribution, which limits the extent of vaporization. This difference has a direct impact on the phase change dynamics, as shown in Fig. 12, where the dual-heater setup (Fig. 12(a)) results in a more complete and uniform phase transition, while the single-heater configuration (Fig. 12(b)) leads to incomplete vaporization due to insufficient thermal energy being delivered to the flow. The implementation of a second heater promotes a more uniform thermal distribution, accelerating the phase transition and increasing the vapor fraction at the nozzle exit. This leads to a higher fluid expansion rate and a corresponding improvement in thrust output.

In the first phase of the numerical study, the fluid behavior was analyzed within the entire device, including the microchannels, heating chamber, and nozzle, to evaluate the interaction between heat transfer, phase transition, and flow dynamics. However, in this configuration, the analysis was limited to the nozzle exit, without considering the discharge domain in an open environment. This could introduce limitations in accurately predicting the expansion conditions of the flow and, consequently, the final thrust value. To improve the nozzle modeling and achieve a more realistic analysis of its performance, the second phase of the study introduced an extended domain downstream of the nozzle, representing the ambient conditions in which the flow expands after exiting. This approach allows for a more accurate capture of pressure recovery, jet expansion, and velocity distribution, which are crucial for precisely determining the thrust. By including this extended domain, the simulation provides a more faithful representation of real operating conditions, ensuring that the computed thrust values align more closely with experimental results. The computational domain for the 3D simulations is comprised of one-quarter of the VLM prototype's final nozzle, extended by an external domain. The outer domain extended 5 times the nozzle height H_{nozzle} upward, 10 times H_{nozzle} downstream, and 50 times the nozzle width W_{nozzle} sideways. This configuration is depicted in Fig. 13, which illustrates the domain extensions and their spatial proportions.

To ensure the accuracy of the simulation results, a mesh independence study was conducted. Several mesh densities were tested, ranging from coarse to fine grids, and the thrust results were compared to identify the optimal grid. The final mesh, consisting of 4 381 200 cells, was selected based on a balance between computational cost and accuracy, ensuring that further refinement had a negligible effect on the thrust results (less than 1% variation). The fluid within the nozzle was modeled as single-phase water vapor, while the outlet was an air mixture of oxygen and nitrogen with standard atmospheric properties. The simulations were conducted for the dual heating configuration, which ensured complete vaporization of the liquid phase before entering the nozzle, thereby preventing phase-change effects within the computational domain and ensuring accurate thrust predictions. The nozzle inlet conditions were obtained from a preliminary numerical simulation of the entire microthruster device, performed without the discharge domain. In this initial simulation, the resulting velocity, temperature, and pressure profiles at the nozzle inlet were extracted and subsequently interpolated as inlet boundary conditions for the dedicated nozzle simulation. This approach ensures that the nozzle operates under conditions that closely replicate those in the full system, providing a more accurate representation of the actual flow field. The extracted flow field data were interpolated onto the

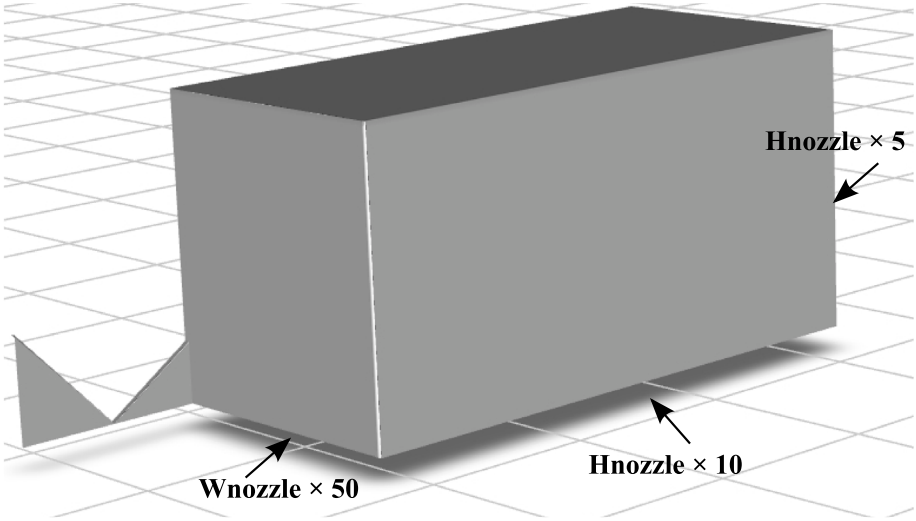

Fig. 13. 3D view of the nozzle with the discharge domain, highlighting the overall geometry and the spatial configuration of the discharge area.

nozzle inlet grid using Fluent's Profile Boundary Condition feature to ensure a smooth transition and avoid numerical discontinuities. The imposed profiles preserved the flow development effects from the upstream simulation, maintaining consistency in velocity, pressure, and turbulence characteristics. To validate the accuracy of the applied inlet conditions, a comparison was performed between the standalone nozzle simulation and the full-device simulation, evaluating velocity magnitude, pressure gradients, and temperature distributions along the nozzle inlet cross-section. Root mean square error analysis was conducted to quantify discrepancies in the interpolated profiles, while turbulence parameters such as turbulent kinetic energy and dissipation rate were also examined. Any significant deviations were addressed through refinements in the interpolation process or grid modifications, ensuring a physically accurate transition and numerical stability across the computational domain. The outlet was set to standard atmospheric conditions, with a pressure of 101 325 Pa and a temperature of 300 K. For the wall boundaries, no-slip conditions were applied, and the walls were assumed to be adiabatic, given the negligible heat transfer in this region. The simulations employed a pressure-based solver, with the SIMPLE algorithm used for pressure-velocity coupling. Second-order discretization schemes were applied to ensure the accuracy of the numerical solution for both momentum and energy equations. The k-ε turbulence model was selected for this study due to its robustness and computational efficiency in capturing the key flow features of the nozzle, particularly in the presence of recirculation zones and flow expansion. This model is well-suited for high-Reynolds-number flows ($Re > 10^5$) and provides a reliable prediction of turbulent kinetic energy and dissipation, making it widely used for industrial applications involving complex flow patterns. While the k-ω SST (Shear Stress Transport) model offers improved accuracy in resolving boundary layer effects and flow separation, it requires a higher near-wall resolution ($y^+ \approx 1$), which significantly increases the number of mesh elements. A more advanced approach, such as Large Eddy Simulation (LES), could provide detailed insights into transient turbulence structures and flow instabilities. However, LES simulations require grid resolutions fine enough to resolve eddies down to the Kolmogorov scale, increasing computational costs by a factor of 10–100× compared to RANS models. Preliminary LES tests on a coarser grid ($\sim 10^7$ elements) showed significant underprediction of turbulence intensity in the nozzle expansion region, necessitating a much finer mesh. To validate the turbulence model choice, a comparative study was conducted between the k-ϵ and k-ω SST models. The results showed less than a 3% difference in thrust calculations and a deviation of less than 2% in pressure distribution at the nozzle exit, confirming that -ϵ provides sufficient accuracy while reducing computational cost by approximately 30% compared to k-ω SST SST. Given these considerations, the k-ϵ model was chosen as the optimal balance between accuracy and computational feasibility for the nozzle flow simulations. Convergence in the numerical simulations was ensured by monitoring residual values and additional flow field parameters. The primary convergence criterion was achieving residuals below 10^{-6} for continuity, momentum, and energy equations, ensuring minimal numerical errors. To further validate convergence, mass and energy balances were checked across the computational domain to confirm that conservation laws were satisfied. The thrust force at the nozzle exit was also monitored during iterations, ensuring it reached a stable value with variations below 1% over 500 iterations. Additionally, surface-averaged pressure and velocity at the nozzle exit were tracked to confirm steady behavior across time steps. These simulations served as the foundation for calculating the thrust generated by the device, crucial for comparing theoretical predictions with experimental results. The formula used for calculating thrust is:

$$F = \dot{m}_e u_e \tag{13}$$

In this context, u_e represents the exit velocity of the fluid and $\dot{m}_e$ represents the mass flow rate at the nozzle exit and is given by:

$$\dot{m}_e = u_e \rho_e A_e \tag{14}$$

where ρ_e is the density of the fluid at the nozzle exit and A_e represents the exit area. The total thrust, based on a quarter of the nozzle, is scaled up by a factor of 4 to represent the full nozzle. Two CFD simulations were conducted using different mass flow rates: one at 1.90×10^{-6} kg/s and the other at 1.70×10^{-6} kg/s, closely replicating the conditions from the experimental campaign in Tests 1 and 4, as detailed in Table 2. The thrust results from these simulations yielded a value of 1.8 mN for Test 1 and a value of 2.7 mN for Test 4, compared to the corresponding experimental values of 1.7 mN and 2.5 mN, respectively. Considering an estimated experimental uncertainty of approximately 7%, the experimental thrust values correspond to 1.7 ± 0.12 mN for Test 1 and 2.5 ± 0.18 mN for Test 4. The CFD-predicted thrust values fall within these uncertainty ranges, confirming good agreement between numerical and experimental results. The observed deviations (5.88% for Test 1 and 8.00% for Test 4) are attributed to sensor accuracy, flow rate fluctuations, and heater power variability. In addition, thrust was calculated in the CFD simulation conducted with only a single heater, resulting in a value of 2.3 mN at a mass flow rate of 1.90×10^{-6} kg/s. Comparing this value with the thrust obtained using two heaters at the same mass flow rate reveals a decrease in performance when only one heater is employed. This observation reinforces earlier findings

regarding the vapor fraction contours, confirming that the addition of a second heater enhances the vaporization process, leading to improved thrust output.

4. Development and validation of a 1D steady-state code to simulate the behavior of the device

The VLM's performance is strongly influenced by microscale boiling instabilities, making active control essential to stabilize temperature and pressure while mitigating the effects of rapid bubble dynamics and flow reversals. Following the CFD simulations, the resulting numerical and experimental data were employed to refine and validate a reduced-order 1D model, developed in line with the methodology proposed in [25]. This model integrates fluid property calculations, spatial and temporal discretization, and heat transfer modeling, enabling the evaluation of different temperature control strategies. Specifically, it was designed to compare various stepwise heating approaches using adaptive PID control techniques. Before incorporating PID control, the model was first validated in its steady-state form, ensuring accuracy and reliability in capturing the system's thermal behavior. Initially, a 1D model was developed to simulate the fluid behavior inside the device and assess its thermal properties and performance parameters. These numerical evaluations were validated against experimental results, ensuring the reliability of the model and enabling a faster and more effective assessment of the device's operation. This section will provide a brief overview of the code's structure, its role in validating experimental results, and its use as the basis for developing an unsteady model implemented with a neural PID controller.

The model solves the steady-state conservation equations for mass, momentum, and energy along the axial direction of the device. The following subsections outline the discretized form of these equations and the corresponding source terms.

Mass conservation. Assuming incompressible flow and steady-state conditions, the mass flow rate is conserved throughout the domain:

$$\dot{m} = \rho_m u A_{\text{cs}} = \text{constant} \tag{15}$$

where ρ_m is the local mixture density, u is the axial velocity, and A_{cs} is the local cross-sectional area of the channel.

Momentum conservation. The pressure drop is associated with viscous losses and is modeled according to the Hagen–Poiseuille approximation for rectangular microchannels:

$$\Delta p = -u \frac{12 \mu_m}{Z_{\text{ch}}^2} \Delta s \tag{16}$$

where μ_m is the dynamic viscosity of the fluid, Z_{ch} is the channel height (or depth), and Δs is the spatial discretization step.

Energy conservation and heat transfer mechanisms. The energy balance in the model captures the enthalpy variation of the fluid due to heat input through the channel wall. The local variation in total enthalpy is described as:

$$\Delta H = \dot{Q}\, \Delta t = \dot{q}\, P_{\text{cs}}\, \Delta s = \left[h_b (T_{\text{wall}} - T_{\text{fl}}) \right] P_{\text{cs}}\, \Delta s \tag{17}$$

where $\dot{q}$ is the convective heat flux per unit area exchanged between the wall and the fluid, P_{cs} is the perimeter of the heat exchange surface, and Δs is the spatial step. The convective heat transfer coefficient h_b is given by:

$$h_b = \frac{\text{Nu} \cdot \kappa_{\text{cond}}}{D_h} \tag{18}$$

with κ_{cond} being the thermal conductivity of the fluid, D_h the hydraulic diameter, and Nu the local Nusselt number based on the flow regime and geometry.

The heat input $\dot{q}(x)$ is not uniform along the channel and is spatially distributed in two heating zones:

$$\dot{q}(x) = \begin{cases} \dfrac{Q_1}{L_1 \cdot A_1} & \text{if } x \in \text{zone 1 (upstream)} \\ \dfrac{Q_2}{L_2 \cdot A_2} & \text{if } x \in \text{zone 2 (downstream)} \end{cases} \tag{19}$$

Here, Q_1 and Q_2 are the power inputs in each zone, and L_i, P_i, A_i define the length and heat exchange geometry of each region. The convective heat flux computed in Eq. (17) is then used to evaluate the wall temperature and enthalpy rise.

External heat losses and net power input. Simultaneously, external heat losses are modeled to account for energy dissipation mechanisms that reduce the effective thermal input. These include:

$$Q_{\text{rad}} = \epsilon \sigma A_{\text{ext}} \left(T_{\text{wall}}^4 - T_{\text{fl}}^4 \right) \tag{20}$$

$$Q_{\text{conv}} = h_{\text{conv}} A_{\text{ext}} \left(T_{\text{wall}} - T_{\text{ambient}} \right) \tag{21}$$

$$Q_{\text{cond}} = k_{\text{Si}} A_{\text{ext}} \frac{T_{\text{wall}} - T_{\text{ambient}}}{L_{\text{ext}}} \tag{22}$$

where A_{ext} is the external surface area, ϵ is the surface emissivity, σ is the Stefan–Boltzmann constant, and T_{ambient} is the ambient temperature.

The **net thermal power** effectively absorbed by the fluid is calculated by subtracting these losses from the total input:

$$P_{\text{net}} = P_{\text{tot}} - \left(Q_{\text{rad}} + Q_{\text{conv}} + Q_{\text{cond}} \right) \tag{23}$$

This net power represents the actual energy available to raise the fluid enthalpy and is used in the calculation of ΔH in Eq. (17), ensuring a physically consistent energy balance across the domain.

It is important to distinguish between the gross thermal power delivered in each heating zone (Q_1 and Q_2) and the convective heat flux $\dot{q}(x)$ that effectively drives the enthalpy increase of the fluid. While Q_1 and Q_2 represent the total power assigned to each section, only a fraction of this power contributes to heating the fluid due to environmental losses.

The actual heat transferred to the fluid per unit surface is modeled as:

$$\dot{q}(x) = h_b(x) \left[T_{\text{wall}}(x) - T_{\text{fl}}(x) \right] \tag{24}$$

where the exchange surface is defined as:

$$A_{\text{exchange}}(x) = P_{\text{cs}}(x) \cdot \Delta s \tag{25}$$

Accordingly, the local power absorbed by the fluid in a given segment is:

$$\dot{Q}(x) = \dot{q}(x) \cdot A_{\text{exchange}}(x) \tag{26}$$

The global net power effectively transferred to the fluid is then obtained by integrating over the heated domain:

$$P_{\text{net}} = \int_{\text{heated zone}} \dot{q}(x) \cdot A_{\text{exchange}}(x)\, dx \tag{27}$$

This ensures a consistent energy balance where only the convective heat actually reaching the fluid contributes to its enthalpy variation, as expressed in Eq. (17).

This ensures that only the thermal power that reaches the fluid contributes to the enthalpy increase and temperature evolution.

After determining the thermal properties at the nozzle inlet, the supersonic expansion of the vapor flow through the nozzle is analyzed to derive the key propulsive parameters. These include the thrust (Eq. (28)) and the specific impulse I_{sp} (Eq. (29)), both of which are critical for assessing propulsion efficiency:

$$F = F_j + F_p = \dot{m} V_{\text{e}} + (p_{\text{e}} - p_{\text{amb}}) A_{\text{e}} \tag{28}$$

$$I_{\text{sp}} = \frac{F}{\dot{m} g_0} \tag{29}$$

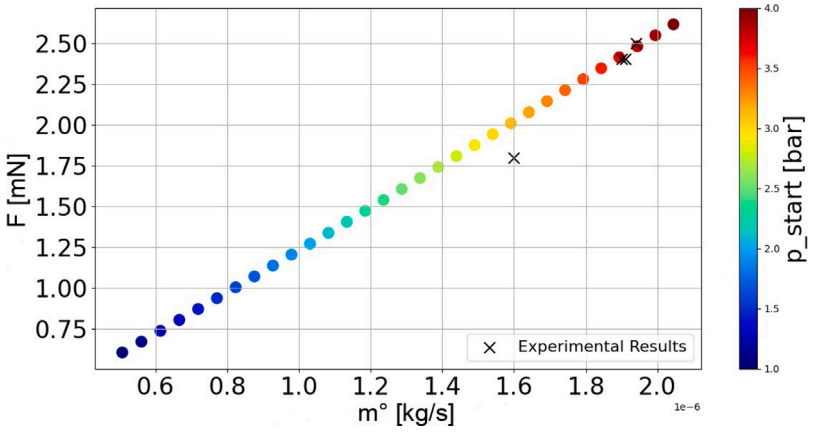

Fig. 14. Relationship between the Thrust and the mass flow rate for different fluid inlet pressure compared with experimental results shown in Table 2. (For interpretation of the references to colour in this figure legend, the reader is referred to the web version of this article.)

Validation of the 1D numerical model

Comparing the numerical results from the 1D model with experimental data is essential to validate the simulation framework and assess its predictive capabilities. This process ensures that the mathematical predictions reliably replicate the real behavior of the device, allowing for virtual performance evaluation and design optimization while minimizing the need for extensive physical testing.

To replicate operating conditions comparable to those of the experimental campaign, the inlet pressure p_{start} was varied from 1 to 4 bar in the simulations, resulting in a range of mass flow rates. Figs. 14 and 15 compare numerical predictions with experimental results from Table 2.

Fig. 14 shows the relationship between mass flow rate and thrust. Each colored point corresponds to a simulation at a given inlet pressure, while the black crosses represent experimental measurements. The thrust–flow rate trend is clearly linear, as expected from quasi-steady, isentropic expansion. Most experimental data points fall very close to the simulation curve, indicating strong consistency between the model and measured thrust values. A minor deviation is observed for Test 1, which lies slightly below the trend. This deviation is attributed to altered initial test conditions, leading to a slightly lower actual mass flow rate than recorded.

Fig. 15 depicts the relationship between fluid thermal power and mass flow rate. Again, the numerical predictions follow a near-linear trend, consistent with the analytical expectation that higher flow rates require proportionally greater thermal input to reach vaporization and expansion conditions. The experimental power values derived from Table 2 (column P_{net}) closely align with the simulation trend. This confirms that the model not only captures the propulsion output but also accurately estimates the energy input needed to generate such output.

Together, these comparisons validate the robustness of the 1D steady-state model in reproducing both mechanical and thermal performance metrics of the device. The model proves capable of predicting thrust and power with acceptable accuracy over the tested operating range. This validates its suitability for use as a reliable surrogate tool in early-stage design and optimization processes.

4.1. Dynamic performance prediction of a dual heating system using a 1D Unsteady-State model with temperature control system

The previously described thermal model was implemented in a Python-based numerical framework, which integrates fluid property calculations, spatial and temporal discretization, heat transfer modeling, and an adaptive PID control system. This computational environment enables a detailed analysis of the thermal response and control effectiveness under varying operational conditions. The computational framework ensures accurate simulation of two-phase heat transfer dynamics while maintaining flexibility for parameter tuning and real-time control adjustments. The numerical framework is structured into modular components, ensuring flexibility, ease of debugging, and adaptability for future developments. The simulation follows a structured approach where fluid dynamics and heat transfer equations are solved iteratively, incorporating real-time control adjustments. The model operates within a time-stepping loop, dynamically adjusting the heater power based on feedback from a simulated thermocouple sensor (RTD3) placed near the nozzle inlet. The code is designed to handle two primary objectives:

1. Thermal modeling of the fluid and wall temperature evolution, using a finite-difference scheme to resolve heat transfer mechanisms.
2. Active temperature control via a PID controller, which continuously adjusts the power input to maintain the desired setpoint temperature. The central simulation script initializes the system parameters, calls the required functions, and iterates over the defined time steps until the convergence criteria are met. The spatial domain of the system is discretized using a finite-difference approach, ensuring a detailed resolution of temperature and pressure fields.

The time evolution follows an explicit time-stepping scheme. Although a nominal time step of $dt = 0.01$ is initially set, the solver dynamically updates the time step at each iteration based on local flow and thermal conditions, ensuring numerical stability and temporal accuracy. The choice of discretizing the spatial domain into 200 nodes and using a total of 5000 time steps was validated a posteriori through a sensitivity analysis, presented in the following section. This analysis confirmed that the adopted resolution is sufficient to accurately capture the system's dynamic response under PID control without introducing excessive numerical error or computational overhead.

At each iteration, the solver performs the following operations:

1. Retrieves updated thermodynamic properties based on temperature and pressure using CoolProp.
2. Solves for convective, conductive, and radiative heat fluxes to determine the net energy balance at each spatial node.
3. Computes the control error by comparing the measured fluid temperature with the setpoint.
4. Applies PID correction, dynamically adjusting heater power to minimize temperature deviation.
5. Records key thermal and control performance metrics for post-processing and validation.

The script initializes the simulation by importing essential libraries, including NumPy for numerical operations, CoolProp for thermodynamic property calculations, and Matplotlib for visualization. The code

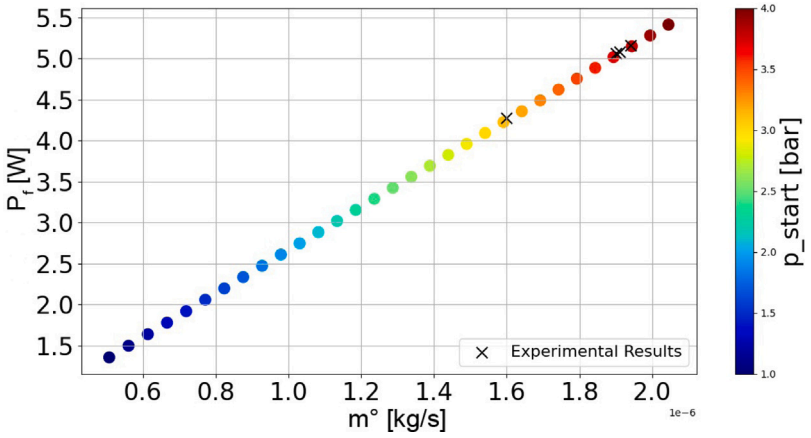

Fig. 15. Relationship between the power and the mass flow rate for different fluid inlet pressure compared with experimental results shown in Table 2.

specifies key physical parameters, such as ambient pressure and temperature, initial fluid conditions, device geometry, thruster material properties, and the power limit. All fluid properties are averaged across the device's cross-sectional area, assuming a homogeneous mixture of liquid and vapor in thermodynamic equilibrium, with properties dynamically computed using CoolProp. The simulation is structured into two main phases: spatial and temporal discretization. The length of the device is divided into discrete spatial steps, where the thermal and geometric properties are calculated at each node. The time-stepping process is governed by an explicit solver, where the time step is determined by considering the average velocity across the device. At each step, the fluid and wall temperatures are updated accordingly. Temperature control is regulated through a time-varying setpoint system defined by the operator. The control loop continuously compares the setpoint with the actual fluid temperature, with a PID controller adjusting the heat input accordingly. The mass flow rate is held constant, utilizing experimentally obtained values as described in Section 2.4. The Nusselt number is set to a constant value of 4.96, ensuring a consistent convective heat transfer model across the simulation. The cycle solves the two-phase flow throughout the entire device, ensuring accurate representation of both liquid and vapor phases in the thermal and performance assessments. The solver accounts for heat losses, including convective, radiative, and conductive mechanisms, subtracting these losses from the total power input to determine the net energy supplied to the fluid. The governing energy balance is:

$$P_{\text{net}} = P_{\text{tot}} - (Q_{\text{rad}} + Q_{\text{conv}} + Q_{\text{cond}}) \tag{30}$$

In addition to simulating the thermal response, the code automatically computes key control performance parameters such as rise time, settling time, and overshoot. These metrics are essential for assessing the efficiency of the control system and optimizing thermal regulation. The PID controller consists of three components: proportional gain (K_P), integral gain (K_I), and derivative gain (K_D). The fluid temperature, measured near the heater, is fed into the controller, where it is compared with the setpoint temperature. The error, defined as the difference between the measured and desired temperatures, is then used to determine the necessary power input required to heat the system and maintain the temperature near the setpoint. The controller adjusts the power input based on the error, ensuring that the system reaches and stabilizes at the desired temperature. Eq. (31) defines the control law that governs the PID controller's operation, which continuously adjusts the power supplied to minimize the error and keep the temperature within the specified range.

$$u(t) = K_P e(t) + K_i \int_0^t e(t)\,dt + K_D \frac{de(t)}{dt} \tag{31}$$

The proportional element K_P helps the controller adjust the error quickly, with the controller reacting in proportion to the magnitude of the error. A large error generates a large response. The K_P alone cannot completely eliminate the steady-state error, as the proportional action requires a persistent error. Although the error decreases with increasing K_P, this can also enhance the system's tendency to oscillate. To solve this problem, the integral control K_i tries to eliminate the residual error by integrating the past values of the error signal. This action drives the steady-state error towards zero. The derivative part, K_D provides an action based on the rate of change of the error, acting as an estimate of the future error. A quantitative assessment of numerical integration errors, including their accumulation over time, is provided in the following subsection in accordance with the methodology of Smirnov et al. [26,27] .

4.1.1. Numerical error estimation

A dedicated sensitivity analysis was conducted to evaluate the influence of spatial discretization on the total heat input, as summarized for the different profiles in Table 4. In particular, for Profile 3, the comparison among simulations with $N_1 = 100$, $N_1 = 200$, and $N_1 = 300$ (taken as the reference case) revealed a maximum relative deviation of approximately 2.4%. This confirms that the spatial discretization error remains well below the commonly accepted 5% threshold, thereby supporting the reliability and consistency of the simulation results. The choice of the temporal discretization was guided by a dedicated sensitivity study aimed at resolving the thermal response of the system during PID-controlled transients. In particular, the goal was to accurately capture the time required for the fluid temperature to reach the target setpoint under various heating conditions. Coarser time resolutions failed to reproduce the detailed shape of the response curve and delayed the identification of rise time and settling time. Conversely, finer discretizations yielded negligible improvements in accuracy while significantly increasing computational cost. Therefore, $n = 5000$ was selected as an optimal compromise to ensure a physically meaningful representation of the control dynamics.

In accordance with the methodology proposed by Smirnov et al. [26], the estimation of integration errors and their accumulation over time is essential in unsteady thermo-fluid simulations. In particular, the relative error of numerical integration in the spatial domain for a one-dimensional case is given by:

$$S_1 \approx \left(\frac{1}{N_1}\right)^{k+1} \tag{32}$$

where k denotes the order of accuracy of the spatial discretization method, in this case $k = 1$. Assuming that only stochastic error accumulates over time, the total accumulated error after n time steps can be approximated as:

$$S_{\text{err}} \approx \sqrt{n} \cdot S_1 \tag{33}$$

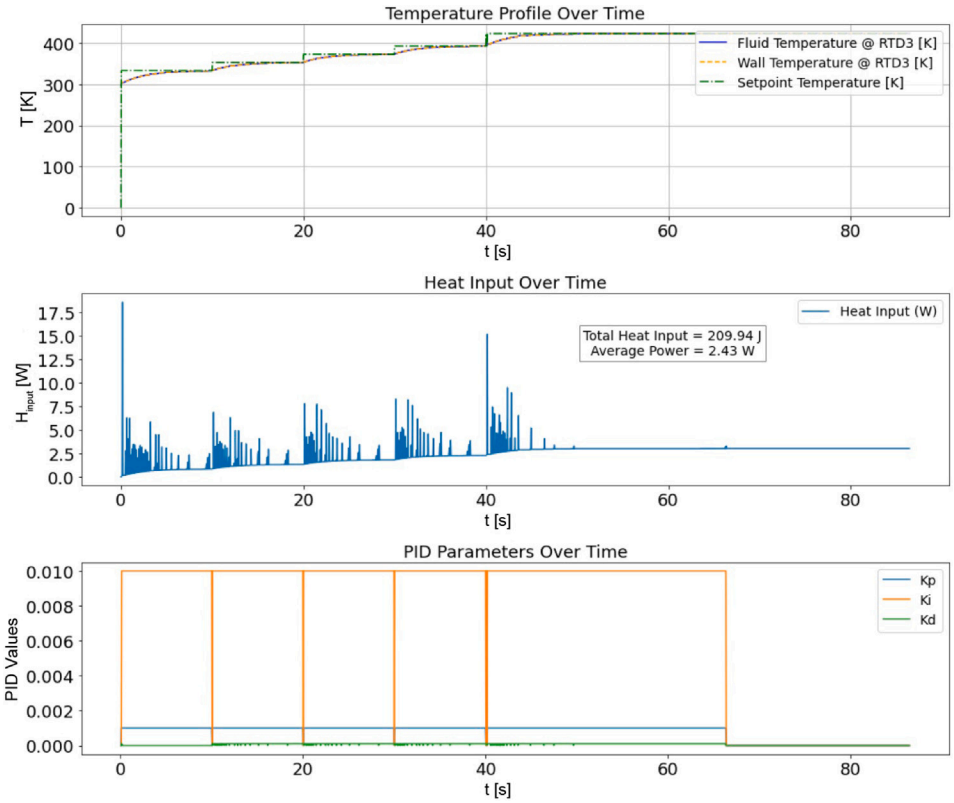

Fig. 16. Step response for Adaptive Neural PID controller for profile 6.

Table 3
Estimated error accumulation and reliability ratio for different spatial resolutions ($n = 5000$).

Mesh Points N_1	S_1	S_{err}	$R_s = \frac{0.05}{S_{\text{err}}}$
100	1.00×10^{-4}	0.0071	7.07
200	2.50×10^{-5}	0.0018	28.28
300	1.11×10^{-5}	0.00079	63.29

According to Smirnov et al. the maximum acceptable total error $S_{\max}$ should generally remain within 1%–5%. In our case, we define the reliability ratio as:

$$R_s = \frac{S_{\max}}{S_{\text{err}}} \tag{34}$$

The computed errors and reliability ratios are summarized in Table 3. As expected, increasing the spatial resolution reduces both the local and total error, resulting in improved reliability margins.

This analysis supports the choice of using at least 200 spatial nodes to ensure numerical reliability in long unsteady simulations.

The calculated values of the reliability ratio R_s confirm that the simulation remains well within the trustworthy range of numerical accuracy for all tested resolutions. Should higher precision be required, increasing the spatial resolution (N_1) or adopting a higher-order scheme ($k > 1$) would allow further reduction of the integration error.

4.1.2. Adaptive neural network PID control

Although PID controllers are widely used in industrial applications, they have limitations, particularly when applied to non-linear and time-varying systems. The initial steady-state analysis was conducted without an active control strategy, revealing that achieving the desired temperature required a power consumption of approximately 4 to 5 W, with no optimization of energy efficiency. This highlighted the necessity of a dynamic control mechanism capable of adapting system parameters in real time to optimize energy use while maintaining stability. To address this, a PID control system was introduced. However, fixed gains for K_P, K_I, and K_D may perform well within a specific operational range but fail to provide optimal results across varying conditions, as observed in the current model. Hence, an Adaptive Neural Network PID Controller was implemented to alter the control gains at different levels depending on the behavior of the system in real time. This adaptive approach is not feasible with conventional PID controllers since they are static, and the system must learn and optimize itself continuously as changes occur. The adaptive PID controller does this by changing the values of its control gains during the simulation. Over the course of the process, the neural network modifies its weights and internal biases and "learns" the most effective PID gains for error minimization. This ability to self-adjust ensures that the system remains optimal under a variety of conditions. Moreover, the adaptive control scheme is very effective for systems with high degree of non-linearity because of its accuracy in temperature control, speed of response, and lower overshoot.

The adaptation process follows these steps:

1. **Error Calculation:** The controller first computes the *error* between the current system state (fluid temperature) and the desired setpoint. The *rate of change of error* is also calculated.
2. **Neural Network Input:** The neural network takes *error* and *error derivative* as input variables.
3. **Weight Calculation & Gain Adaptation:** The network applies a *linear transformation* using *pre-trained weights and biases* to generate the new values of K_P, K_I, K_D. The new gains are constrained within a predefined range.
4. **PID Control Computation:** The updated PID gains are used to compute the *control action*, Eq. (31).
   The neural network then *adjusts its weights dynamically* using a *gradient-based learning process* to optimize these values in real time.

5. **Control Constraints and Learning Process:** To prevent instability and excessive fluctuations, the PID gain values are clipped within predefined limits:

   - $0 \leq K_P \leq 0.001$
   - $0 \leq K_I \leq 0.01$
   - $0 \leq K_D \leq 0.0001$

   These limits were empirically determined to balance fast response, minimal overshoot, and energy efficiency. The learning rate was set to 0.5 to balance adaptability and stability. A too-high learning rate leads to excessive fluctuations, while a too-low value slows down adaptation.

During initialization, small random values were assigned to the **weights** ($\sim\mathcal{N}(0, 0.005)$) to prevent large fluctuations at the start, while **biases** were initialized to zero. It is important to specify the role of weights and biases:

- Weights: coefficients associated with each input; each input is multiplied by a specific weight determining how much each input contributes to the final output.
- Bias: additional value that is added to the output of the weighted sum of the inputs. Each neuron in a neural network has its own bias. This value allows the neural network to move the activation function, up or down, avoiding it passing through the origin.

The weights and biases were updated using a **gradient-based optimization process**:

$$\text{weights} += \text{learning rate} \times \text{gradient output} \tag{35}$$

This ensured that the PID gains dynamically adjusted in response to the system's real-time behavior. With the implementation of the Adaptive Neural PID Controller, different temperature profiles could be analyzed, with the goal of identifying the profile that provides the lowest average power P_{avg} and energy consumption profile E_{tot}. The evaluation was also carried out considering the main response parameters of the system, such as τ_{rise}, τ_{set} and $\%OS$. To evaluate the effectiveness of the adaptive PID controller, the following **key performance indicators (KPIs)** were monitored:

- τ_{rise} - *Rise Time:* Time taken to reach 90% of the final temperature.
- τ_{set} - *Settling Time:* Time taken for the system to stabilize within 2% of the final value.
- P_{avg} - *Average Power Consumption.*
- E_{tot} - *Total Energy Consumption.*

The objective was to minimize P_{avg} and E_{tot} while ensuring fast rise and settling times with minimal overshoot.

By leveraging an **adaptive learning approach**, the implemented control strategy significantly improves **thermal stability, energy efficiency, and system responsiveness**, making it a robust solution for the dynamic conditions of the VLM.

Analyzing the results shown in Tables 4 and 5, the system response is more stable when the temperature change is gradual over time. However, it is important to note that excessive setpoint variation can not only improve system responsiveness, but also results in significantly higher power consumption. This is because rapid oscillations require additional power to keep the system within the desired thresholds. Therefore, a trade-off between stability and power consumption is evident, suggesting the need to optimize temperature profiles to achieve an optimal balance between performance and energy efficiency. Analyzing the results shown in Tables 4 and 5, the system response is more stable when the temperature change is gradual over time. However, it is important to note that excessive setpoint variation can not only improve system responsiveness, but also results in significantly higher power consumption. This is because rapid oscillations require additional power to keep the system within the desired thresholds.

Table 4
System response parameters for different temperature profiles.

Profile	T_{set} [K]	Time step [s]	τ_{rise} [s]	τ_{set} [s]
Profile 1	50	$0 \leq t < 10$	4.97	8.95
	150	$t \geq 10$	6.14	12.28
Profile 2	50	$0 \leq t < 10$	4.80	8.69
	100	$10 \leq t < 20$	5.40	8.34
	150	$t \geq 20$	5.66	26.37
Profile 3	60	$0 \leq t < 10$	5.36	9.47
	100	$10 \leq t < 20$	5.24	9.94
	145	$20 \leq t < 30$	4.84	7.95
	180	$t \geq 30$	6.23	26.54
Profile 4	120	$0 \leq t < 30$	5.97	12.06
	150	$t \geq 30$	7.09	25.81
Profile 5	45	$0 \leq t < 10$	4.58	8.30
	90	$10 \leq t < 30$	5.58	10.25
	130	$30 \leq t < 50$	5.10	9.86
	150	$t \geq 50$	7.78	24.34
Profile 6	60	$0 \leq t < 10$	5.27	9.64
	80	$10 \leq t < 20$	6.01	8.21
	100	$20 \leq t < 30$	6.01	8.21
	120	$30 \leq t < 40$	6.01	8.21
	150	$t \geq 40$	6.79	26.20

Table 5
P_{avg} and E_{tot} for different profiles.

TEST	P_{avg} [W]	E_{tot} [J]
Profile 1	2.77	239.82
Profile 2	2.67	230.77
Profile 3	3.15	272.38
Profile 4	2.85	246.00
Profile 5	2.45	211.83
Profile 6	2.42	209.43

Therefore, a trade-off between stability and power consumption is evident, suggesting the need to optimize temperature profiles to achieve an optimal balance between performance and energy efficiency. For this reason, the profile identified as best in terms of E_{tot} is profile 6 (see Fig. 16), which represents the right trade-off between faster system response times and lower energy consumption. This profile allows the system to maintain good stability while reducing the energy required for its operation, thus making it a preferable option for practical applications. Compared to the power consumption observed without control, which was around 4–5 W both experimentally and numerically, the implementation of the adaptive PID controller has resulted in power consumption values that are approximately half of those observed in the uncontrolled system. This reduction is particularly significant for profile 6, where the optimized stepwise heating strategy ensures minimal power expenditure while maintaining stable thermal conditions. This demonstrates the effectiveness of the PID-based control strategy in achieving an optimal balance between energy efficiency and system stability. For this reason, the profile identified as best in terms of E_{tot} is profile 6 (see Fig. 16), which represents the right trade-off between faster system response times and lower energy consumption. This profile allows the system to maintain good stability while reducing the energy required for its operation, thus making it a preferable option for practical applications.

5. Conclusion

This study presents an integrated numerical and experimental analysis of a Vaporizing Liquid Microthruster featuring a novel dual heating configuration and an adaptive control strategy. The objective was to enhance thermal control, mitigate flow boiling instabilities, and optimize the device's performance for small satellite propulsion applications.

Key novelties of this work include:

- **A redesigned device geometry**, which improves heat distribution and enhances vaporization efficiency, leading to superior thermal and propulsive performance.
- **A dual-heating dual-chamber design**, which decouples the boiling and superheating phases, reducing thermal stresses and providing greater control over fluid phase change.
- **A validated 1D numerical model**, enabling the comparison of different non-stationary heating strategies to optimize power consumption and temperature regulation.
- **An adaptive Neural Network control strategy**, dynamically adjusting proportional integrative e derivative gains in real time, ensuring energy-efficient heating profiles.

The results demonstrate that the new vaporizing liquid microthruster design and the adaptive pulsed heating approach provide greater thermal stability and improved energy efficiency compared to conventional single-heater configurations. The adaptive proportional-intra-negative control strategy effectively reduces power consumption, particularly for Profile 6, which achieved the best trade-off between fast response times and energy efficiency. Compared to uncontrolled heating, which required 4–5 W, the control strategy reduced power consumption by approximately 50%, confirming its effectiveness in optimizing the heating process. This work introduces a significant advancement in microthruster technology, combining innovative geometry, dual heating, and intelligent control strategies to achieve superior performance. Future research will focus on refining the control algorithms, integrating machine learning-based optimization, and further validating the system under space-relevant operating conditions to push the technology readiness level of these devices beyond 5.

CRediT authorship contribution statement

Angelica Maria Toscano: Writing – review & editing, Writing – original draft, Software, Investigation, Formal analysis. **Daan Kortleven:** Validation, Investigation, Data curation. **Donato Fontanarosa:** Supervision, Software, Methodology, Investigation, Data curation, Conceptualization. **Miriam Basile:** Methodology, Investigation, Data curation. **Guido Marseglia:** Writing – original draft, Methodology, Data curation. **Maria Rosaria Vetrano:** Methodology, Investigation, Formal analysis, Conceptualization. **Johan Steelant:** Supervision, Funding acquisition, Formal analysis, Conceptualization. **Luca Francioso:** Methodology, Investigation, Formal analysis, Data curation, Conceptualization. **Maria Grazia De Giorgi:** Writing – review & editing, Methodology, Investigation, Funding acquisition, Conceptualization.

Declaration of competing interest

The authors declare that they have no known competing financial interests or personal relationships that could have appeared to influence the work reported in this paper.

Acknowledgment

The authors gratefully acknowledge the financial support of the European Space Agency from the Open Space Innovation Program (OSIP) – Open Discovery Ideas, grant No. 4000 135973/21/NL/GLC/my.

References

[1] D. Fontanarosa, L. Francioso, M.G. De Giorgi, M.R. Vetrano, MEMS vaporazing liquid microthruster: A comprehensive review, Appl. Sci. 11 (19) (2021) 8954.
[2] J. Mueller, W. Tang, A. Wallace, R. Lawton, W. Li, D. Bame, I. Chakraborty, Design, analysis and fabrication of a vaporizing liquid micro-thruster, in: 33rd Joint Propulsion Conference and Exhibit, 1997, p. 3054.
[3] J. Mueller, D. Bame, I. Chakraborty, A. Wallace, W. Tang, R. Lawton, Proof-of-concept demonstration of a vaporizing liquid micro-thruster, in: 34th AIAA/ASME/SAE/ASEE Joint Propulsion Conference and Exhibit, 1998, p. 3924.
[4] J. Mueller, Vaporizing liquid microthruster concept: Preliminary results of initial feasibility studies, Micropropuls. Small Spacecr. 187 (2000) Chap–8.
[5] E. Mukerjee, A. Wallace, K. Yan, D. Howard, R. Smith, S. Collins, Vaporizing liquid microthruster, Sens. Actuators Phys. 83 (1–3) (2000) 231–236.
[6] D.K. Maurya, S. Das, S. Lahiri, Silicon MEMS vaporizing liquid microthruster with internal microheater, J. Micromech. Microeng. 15 (5) (2005) 966.
[7] P. Kundu, T.K. Bhattacharyya, S. Das, Design, fabrication and performance evaluation of a vaporizing liquid microthruster, J. Micromech. Microeng. 22 (2) (2012) 025016.
[8] X. Ye, F. Tang, H. Ding, Z. Zhou, Study of a vaporizing water micro-thruster, Sens. Actuators Phys. 89 (1–2) (2001) 159–165.
[9] M.A. Silva, D.C. Guerrieri, H. van Zeijl, A. Cervone, E. Gill, Vaporizing liquid microthrusters with integrated heaters and temperature measurement, Sens. Actuators Phys. 265 (2017) 261–274.
[10] K. Karthikeyan, S. Chou, L. Khoong, Y. Tan, C. Lu, W. Yang, Low temperature co-fired ceramic vaporizing liquid microthruster for microspacecraft applications, Appl. Energy 97 (2012) 577–583.
[11] K.H. Cheah, K.-S. Low, Fabrication and performance evaluation of a high temperature co-fired ceramic vaporizing liquid microthruster, J. Micromech. Microeng. 25 (1) (2014) 015013.
[12] C.-C. Chen, C.-W. Liu, H.-C. Kan, L.-H. Hu, G.-S. Chang, M.-C. Cheng, B.-T. Dai, Simulation and experiment research on vaporizing liquid micro-thruster, Sens. Actuators Phys. 157 (1) (2010) 140–149.
[13] J. Cen, J. Xu, Performance evaluation and flow visualization of a MEMS based vaporizing liquid micro-thruster, Acta Astronaut. 67 (3–4) (2010) 468–482.
[14] P.-W. Kwan, X. Huang, X. Zhang, Design and testing of a microelectromechanical-system-based high heat flux vaporizing liquid microthruster, Acta Astronaut. 170 (2020) 719–734.
[15] D. Fontanarosa, D. Van Langenhove, M.A. Signore, M.G. De Giorgi, L. Francioso, J. Steelant, M.R. Vetrano, Towards an optimized heat transfer process in vaporizing liquid microthrusters using pulsed heating control, Acta Astronaut. 219 (2024) 48–59.
[16] D. Fontanarosa, C. De Pascali, M.G. De Giorgi, P. Siciliano, A. Ficarella, L. Francioso, Fabrication and embedded sensors characterization of a micromachined water-propellant vaporizing liquid microthruster, Appl. Therm. Eng. 188 (2021) 116625.
[17] R.J. Moffat, Describing the uncertainties in experimental results, Exp. Therm. Fluid Sci. 1 (1) (1988) 3–17.
[18] W. Lee, A Pressure Iteration Scheme for Two-Phase Modeling, Technical Report LA-UR 79-975, Los Alamos, New Mexico, 1979.
[19] Q. Shen, D. Sun, S. Su, N. Zhang, T. Jin, Development of heat and mass transfer model for condensation, Int. Commun. Heat Mass Transfer 84 (2017) 35–40.
[20] D. Lorenzini, Y.K. Joshi, Computational fluid dynamics modeling of flow boiling in microchannels with nonuniform heat flux, J. Heat Transf. 140 (1) (2018) 011501.
[21] V. Tyurenkova, M. Smirnova, L. Stamov, Mathematical modeling of nonequilibrium combustion processes in a liquid rocket engine, Acta Astronaut. 225 (2024) 454–466.
[22] V. Tyurenkova, M. Smirnova, V. Nikitin, Two-phase fuel droplet burning in weightlessness, Acta Astronaut. 176 (2020) 672–681.
[23] N. Smirnov, V. Pushkin, V. Dushin, A. Kulchitskiy, Microgravity investigation of laminar flame propagation in monodisperse gas-droplet mixtures, Acta Astronaut. 61 (2007) 626–636.
[24] V. Betelin, N. Smirnov, V. Nikitin, V. Dushin, A. Kushnirenko, V. Nerchenko, Evaporation and ignition of droplets in combustion chambers modeling and simulation, Acta Astronaut. 70 (2012) 23–35.
[25] M. De Giorgi, D. Fontanarosa, A novel quasi-one-dimensional model for performance estimation of a Vaporizing liquid microthruster, Aerosp. Sci. Technol. 84 (2019) 1020–1034.
[26] N. Smirnov, V. Betelin, V. Nikitin, L. Stamov, D. Altoukhov, Accumulation of errors in numerical simulations of chemically reacting gas dynamics, Acta Astronaut. 117 (2015) 338–355.
[27] N. Smirnov, V. Betelin, R. Shagaliev, V. Nikitin, I. Belyakov, Y. Deryuguin, S. Aksenov, D. Korchazhkin, Hydrogen fuel rocket engines simulation using LOGOS code, Int. J. Hydrog. Energy 39 (20) (2014) 10748–10756.